

INVESTIGATIONS INTO A NON-CONTACTING DIRECT  
MEASUREMENT OF WAVENUMBER DISTRIBUTION  
FOR A VIBRATING SURFACE

by

ROBERT S. BETROS

*B.S., Aerospace Engineering  
Boston University  
(1987)*

Submitted to the Department of  
Mechanical Engineering  
in Partial Fulfillment of the Requirements of  
the Degree of  
MASTER OF SCIENCE IN MECHANICAL ENGINEERING

at the  
MASSACHUSETTS INSTITUTE OF TECHNOLOGY

August 1, 1989

© Massachusetts Institute of Technology, 1989  
All rights reserved

Signature of Author \_\_\_\_\_  
Department of Mechanical Engineering  
August 1, 1989

Certified \_\_\_\_\_  
Richard H. Lyon  
Thesis Supervisor

Accepted by \_\_\_\_\_  
Ain A. Sonin  
Chairman, Department Committee

MASSACHUSETTS INSTITUTE  
OF TECHNOLOGY

MAR 13 1990

LIBRARIES

ARCHIVES

INVESTIGATIONS INTO A NON-CONTACTING DIRECT  
MEASUREMENT OF THE WAVENUMBER DISTRIBUTION  
FOR A VIBRATING SURFACE

by

Robert S. Betros

Submitted to the Department of Mechanical Engineering on  
August 1, 1989 in partial fulfillment of the requirements of  
the Degree of Master of Science in Mechanical Engineering

ABSTRACT

Sound radiation from vibrating surfaces is of major concern in the field of structural acoustics. The amplitude and frequency of vibration of each surface wave present as well as the distribution of surface waves is needed to determine sound radiation. A non-contacting method to obtain a direct measurement of this information is presented. This method utilizes the diffraction characteristics of an incident wave field on a vibrating surface to measure its complete wavenumber distribution. Investigations into two different types of incident wave fields are performed and the hardware to fabricate a measurement system for each is specified. Experimental results of the measured wavenumber distribution for a single mode of vibration of a clamped-clamped plate are presented. The measured wavenumbers present on the vibrating plate agreed well with the theory. The measured amplitudes of these wavenumbers, however, was less than expected in each case. The results of this work clearly indicate the possibility of using this measurement method to measure the complete wavenumber distribution of a vibrating surface.

Thesis Supervisor : Richard H. Lyon

Title : Professor of Mechanical Engineering

## ACKNOWLEDGEMENTS

Thanks to Professor Richard H. Lyon for his supervision and guidance throughout this project. His influence was the highlight of my MIT education.

Special thanks go to The Office of Naval Research / DARPA for providing financial support for my work.

Thanks also go to Dr. Michael Hersher and Dr. Jerry Wenjtes of OPTRA, Inc. for their extremely helpful insights during the earlier stages of this thesis.

Thanks to my friends and fellow lab members for our technical and non-technical discussions which really helped me complete this work. They are

Smail Boudarba	Lan Liu
Djamil Boulahbal	Kevin McCoy
Craig Gardner	Scott Miller
Yuksel Gur	Larry Olivieri
Kay Herbert	Charles Oppenheimer
Akio Kinoshita	Bradley Starobin
Nobuo Kolzumi	Mary Toscano
Alfred Levi	Linda Ystueta

Finally, and most importantly, to my parents for their never-ending support throughout my entire life.

## TABLE OF CONTENTS

	page
Abstract	2
Acknowledgements	3
Table of Contents	4
List of Figures	7
1. Introduction	10
1.1 Introduction to Structural Acoustics	10
1.2 The Need for Research	10
1.3 Research Goals	12
1.4 Thesis Organization and Content	14
2. Theoretical Development	15
2.1 Introduction	15
2.2 The Diffraction Formula	17
2.3 Fresnel Diffraction	19
2.4 Fraunhofer Diffraction	20
2.5 The Aperture Function	21
2.6 The Rectangular Aperture	22
2.7 The Comb Function	23
2.8 The Phase Grating	27

	page
2.9 The Complex Phase Grating	38
2.10 The Dynamic Complex Phase Grating	41
3. Preliminary Experiments	42
3.1 Determination of the Type of Incident Wave	42
3.2 The Prototype Laser Experiment	43
3.3 Preliminary Findings	45
4. Final Experiments	47
4.1 Choosing the Alternate Wave Field	47
4.2 Initial Ultrasonic Transducer Choice	48
4.3 The Ultrasonic Measurement System	51
4.4 The Test Surface	53
4.5 Generating and Measuring a Mode of Vibration	55
5. Results	67
5.1 Experimental Observations	67
5.2 Diffraction Pattern Measurements	68
6. Conclusions and Future Recommendations	70
6.1 Discussion of Results	70
6.2 Recommendations for Future Research	71

	page
References	75
Appendix A	77
Appendix B	85
Appendix C	88
Appendix D	92

## LIST OF FIGURES

		page
FIG 2.01	Diffraction effect motivating the work in this thesis.	16
FIG 2.02	Coordinate system and notation used in diffraction equations.	17
FIG 2.03	The one-dimensional sinc function.	23
FIG 2.04	The one-dimensional comb function.	24
FIG 2.05	The fourier transform of the one-dimensional comb function.	26
FIG 2.06	The two-dimensional phase grating.	28
FIG 2.07	Geometric representation of the constant and variable phase terms.	29
FIG 2.08	The first five integer orders of the Bessel function of the first kind.	33
FIG 2.09	Calculated diffraction pattern for a one-dimensional phase grating with surface wavelength equal to $10 \lambda_i$ . The distances $r_o$ and $s_o$ are equal to $400 \lambda_i$ .	37
FIG 2.10	Example of a triangular shaped wavenumber distribution.	39
FIG 2.11	Calculation of the diffraction pattern for the triangular surface wavenumber distribution. This shows the effect of the overlapping of the higher order Bessel functions of the individual phase gratings, which form the wavenumber distribution.	39
FIG 2.12	Example of a sinusoidal shaped wavenumber distribution.	40

	page
FIG 2.13	Calculation of the diffraction pattern for the sinusoidal surface wavenumber distribution. This shows the effect of the overlapping of the higher order Bessel functions of the individual phase gratings, which form the wavenumber distribution. 40
FIG 3.01	Schematic of the prototype laser experiment. 43
FIG 3.02	Photograph of the prototype laser experiment. 44
FIG 4.01	Schematic of the ultrasonic measurement system. 51
FIG 4.02	Photograph of the ultrasonic measurement system. 52
FIG 4.03	Drive point conductance measurement for the plate under test. 55
FIG 4.04	Schematic of the mode shape measurement system. 57
FIG 4.05	Photograph of the mode shape measurement system. 57
FIG 4.06	Measured horizontal mode shape of the test surface at a vibration frequency of 1234 hz. 58
FIG 4.07	Measured horizontal mode shape of the test surface at a vibration frequency of 1706 hz. 59
FIG 4.08	Measured horizontal mode shape of the test surface at a vibration frequency of 3202 hz. 59
FIG 4.09	Calculated wavenumber distribution for the third fundamental mode of vibration of the test surface. 61



		page
FIG 4.10	Calculated diffraction pattern for the third fundamental mode of vibration using a 40 khz sound wave.	62
FIG 4.11	Zoom view of the calculated diffraction pattern for the third fundamental mode of vibration using a 40 khz sound wave.	62
FIG 4.12	Calculated diffraction pattern for the third fundamental mode of vibration using a 75 khz sound wave.	63
FIG 4.13	Zoom view of the calculated diffraction pattern for the third fundamental mode of vibration using a 75 khz sound wave.	63
FIG 4.14	Calculated wavenumber distribution for the sixth fundamental mode of vibration of the test surface.	64
FIG 4.15	Calculated diffraction pattern for the sixth fundamental mode of vibration using a 40 khz sound wave.	64
FIG 4.16	Zoom view of the calculated diffraction pattern for the sixth fundamental mode of vibration using a 40 khz sound wave.	65
FIG 4.17	Calculated diffraction pattern for the sixth fundamental mode of vibration using a 75 khz sound wave.	65
FIG 4.18	Zoom view of the calculated diffraction pattern for the sixth fundamental mode of vibration using a 75 khz sound wave.	66
FIG 5.01	Diffraction pattern measurements using the 40 khz transducer.	69
FIG 5.02	Diffraction pattern measurements using the 75 khz transducer.	69

## **1. INTRODUCTION**

### **1.1 Introduction to Structural Acoustics**

Sound radiation from vibrating structures is of major concern in the field of structural acoustics. Very often the design engineer is looking for ways in which he can improve his design so as to make it radiate sound less efficiently. Excessive sound radiated by naval vessels is an important problem since this sound permits the acoustic detection and identification of the vessel. In room acoustics, the enclosing surfaces of the room need to be designed so as to minimize sound transmission into or out of the room. Minimizing the sound radiation from a vibrating surface is accomplished by reducing or eliminating those surface waves which are well coupled to sound in the fluid in contact with the surface. In fact, any vibrating surface which produces unwanted sound or accepts unwanted vibration from an incident sound wave can be redesigned to minimize the coupling between the vibration and the acoustic field provided that the complete vibration characteristics are known.

### **1.2 The Need for Research**

To determine the characteristics of the structure which are causing the unwanted radiation, a complete knowledge of the components of its vibration is required. The amplitude and frequency of vibration at a few discrete points on

the vibrating surface are not enough to determine the radiated sound. A knowledge of each surface wave present as well as the distribution of surface waves is needed to determine sound radiation. This is important since the radiated sound is due primarily to the surface waves which are well coupled to the acoustic field. The vibration is described by its complete wavenumber distribution, which is the amplitude and frequency content of each surface wave.

Current measurement techniques employ a point by point measurement of some type, whether by scanning across the surface with a single sensor or by using an array of sensors. The vibration characteristics of each point in the scan are then used to obtain the wavenumber distribution in the following way. The maximum amplitude of the vibration at each point is acquired and this information defines the spatial shape of the surface. Then, the fourier transform of this mode shape is calculated. It's this spatial transform which is the wavenumber distribution for the mode shape in question at the frequency of the vibration. Unfortunately, for two dimensional surfaces this process is quite time consuming and requires some minor signal processing.

There are also some problems introduced by the type of sensor which is used to make the measurement. A sensor which contacts the surface, such as an accelerometer, will locally load the vibrating surface in such a way that it will slightly affect the vibration amplitude at that point. This effect becomes even more important when arrays of surface contacting sensors are used. Since the spatial resolution of the surface waves being measured depends on the spacing

between points in the array, a trade-off develops between the surface wave resolution and the altering of the surface vibration from loading effects. The problem associated with non-contacting surface sensors, such as a laser interferometer, are that these sensing systems typically consist of expensive components and require extremely accurate alignment. This forces the experiments to be carried out under laboratory conditions and the measurement method tends to be cumbersome for measuring large structures in the field.

A great need exists for a direct non-contacting method to acquire the complete wavenumber distribution of a vibrating surface. Much of the research being performed in structural acoustics is being carried out without this information due to either the high cost of a computer system capable of handling large arrays of sensors, or the amount of time required to make the point by point scan. The research which is making use of this information could be performed quicker with a more direct measurement method. The presence of a direct non-contacting method to measure the complete wavenumber distribution of a vibrating surface will aid research in the field of structural acoustics.

### **1.3 Research Goals**

The above discussion describes the motivation behind the work performed in this thesis and establishes the desired result of any research in this area. The goal of this thesis research is simply to investigate the possibility of using the diffraction characteristics of an incident wave field on a vibrating surface to

measure the complete wavenumber distribution. The apparent advantages of using this type of measuring method are the following. The measurement is made without contacting the test surface. The spatial information in the wavenumber distribution is measured directly rather than calculated from the surface mode shape. The measurement method could be employed out of the laboratory and even underwater. Finally, the time required to make the measurement could be substantially reduced. There are, however, some questions of the feasibility of making the measurement in this way, and it is these questions which will be investigated in the course of this thesis.

Upon completion of this research, the following will be accomplished;

- 1) The rules under which this measurement method may be employed will be defined.
- 2) An investigation into the type of incident wave field to be used will be performed.
- 3) The appropriate sensors to create and sense the wave field will be determined.
- 4) Preliminary measurements of the wavenumber distribution of a clamped-clamped plate will be made and compared to measurements made with a conventional point by point scan.

In future work, this method should be thoroughly tested on an existing model in the laboratory whose wavenumber distribution characteristics are known

quite well. This test will prove the feasibility of making field measurements on "real" surfaces with this method.

#### **1.4 Thesis Organization and Content**

The goals described above describe the content of this research. Chapter 2 describes, in detail, the proposed method of measurement, and discusses its shortcomings which become evident in the theoretical development. Chapter 3 displays the investigation into the choice of incident wave field to use, and presents some qualitative results of some preliminary experiments. Chapter 4 outlines the prototype measurement system defined from theory and the experimental methods. Chapter 5 presents the results of some measurements made with this system. Finally, Chapter 6 presents the conclusions arrived at from this research along with some recommendations for future work on this measurement system.

## 2. THEORETICAL DEVELOPMENT

### 2.1 Introduction

As stated in Chapter 1, the aim of this research is to investigate the possibility of using the diffraction characteristics of an incident wave field on a vibrating surface to measure its complete wavenumber distribution. The basic idea motivating the work in this thesis is the following. If a wave field of wavelength  $\lambda_i$  is normally incident on a statically deflected sinusoidal surface of wavelength  $\Lambda$ , then the resulting diffraction pattern will contain intensity maxima at discrete distances proportional to the surface wavelength (See Figure 2.1). The wavenumber resolution in the diffraction pattern is inversely related to the number of full surface waves present on the test surface. It is this phenomenon which produces the surface wavenumber distribution directly.

In the theoretical development which follows, the incident wave field is assumed to be generic since the theory applies equally well to any traveling wave field. The basic ideas of the following discussion have been adapted from [1], [2], [3], [4], [5], and [6] and extended to meet this particular application of vibration measurement.

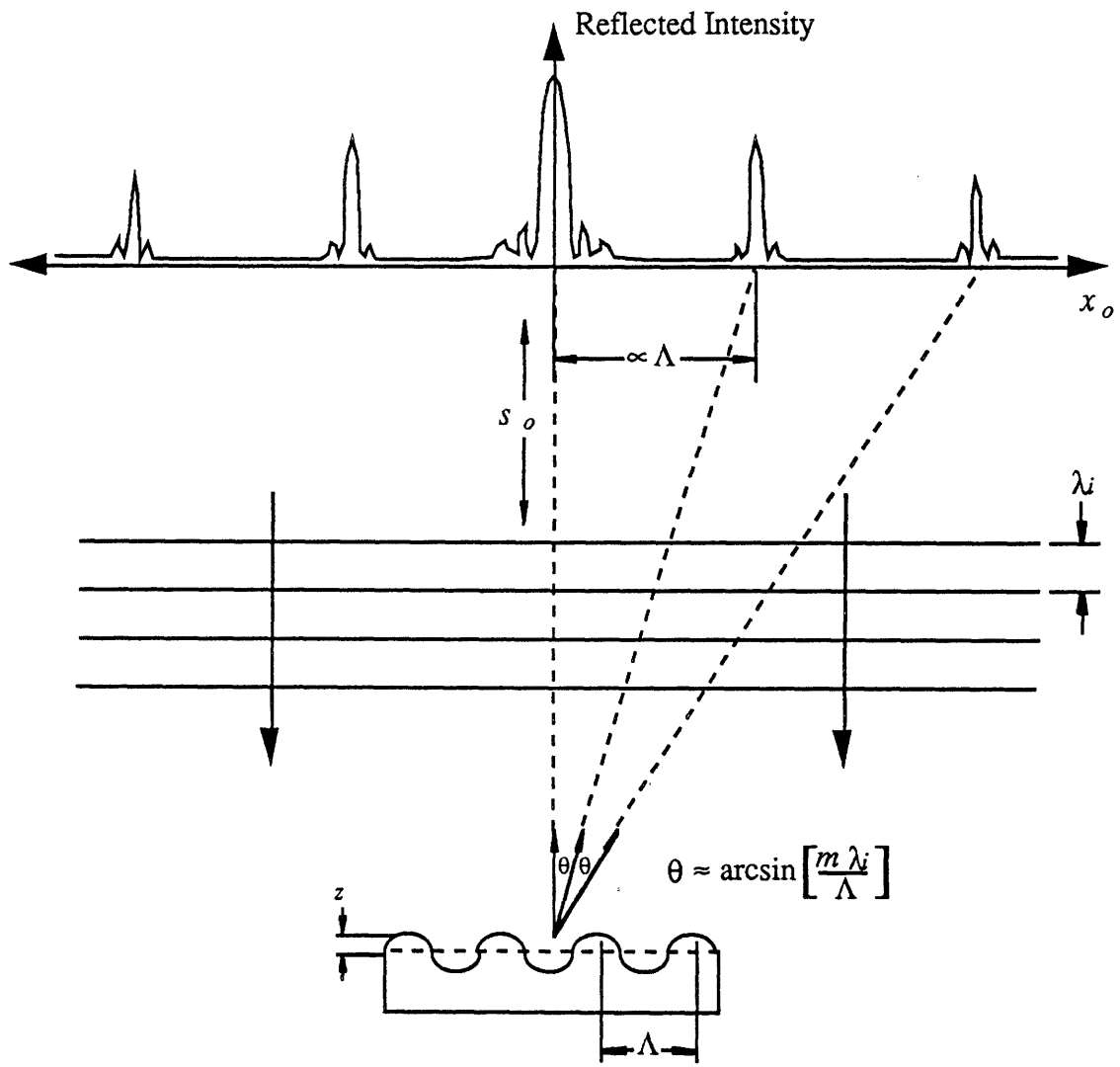


Figure 2.01 Diffraction effect motivating the work in this thesis.



## 2.2 The Diffraction Formula

The expression which governs the distribution of energy produced by a traveling wave field which passes through a small opening in a screen can be arrived at by considering the situation displayed in Figure 2.2. All of the variables locating position in the plane of the source will have no subscripts, whereas those locating points in the plane of the aperture will have the subscript ( $0$ ). The variables locating points the plane of the diffraction pattern will be indicated with a prime symbol ( $'$ ). The energy which originates at a point  $P$  in the source plane travels through the small aperture in the screen and arrives at point  $P'$  in the plane of the diffraction pattern. There are some assumptions which must be stated before the discussion is continued. The distances between the screen and points  $P$  and  $P'$  must be large compared to the size of the aperture and the direct path between points  $P$  and  $P'$  must also be very near to a straight line.

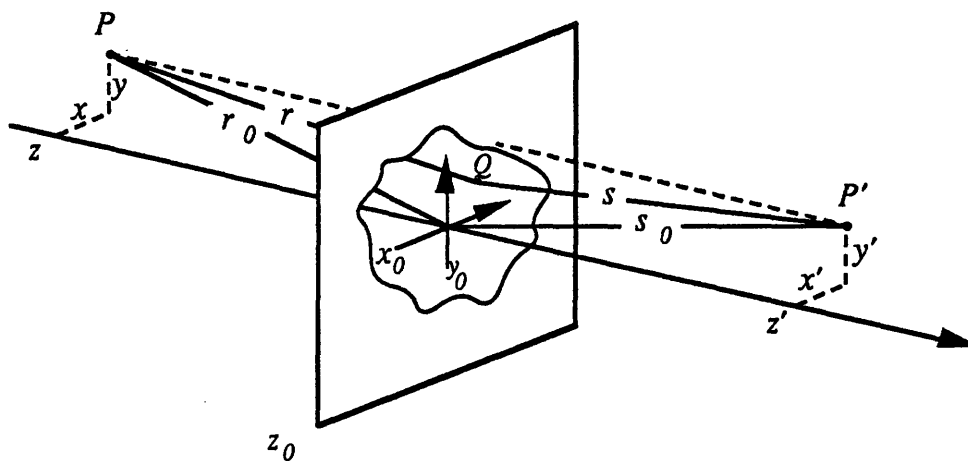


Figure 2.02 Coordinate system and notation used in diffraction equations.

Let the expression for the traveling wave incident on the screen be

$$\hat{U}_o = \frac{U_o}{r} e^{i(\omega t - kr)} \quad (2.1)$$

where  $U_o$  is the amplitude at unit distance from the source  
 $k$  is the wavenumber of the incident wave  $k=2\pi/\lambda$   
 $\omega$  is the frequency of the traveling wave

Huygens' principle, which states that every point on each wavefront is the source of a new spherical wave, can be applied to each point in the aperture. The presence of the incident wavefronts on the aperture creates elemental Huygens' wavelets at all points  $Q$  in the aperture. There are varying path lengths between each wavelet and a single point in the plane of the diffraction pattern. These path differences generate phase differences between each of the elemental spherical waves and cause some amount of cancellation or reinforcement at point  $P'$ . An integral across the face of the aperture over each of these elemental Huygens' wavelets may be calculated and results in the intensity at point  $P'$ . The diffraction pattern is calculated by doing this for each point in the plane  $z=z'$ . The following is the basic diffraction equation for an incident wave front passing through an arbitrary aperture and yields the amplitude of the disturbance at any point  $P'$  in the plane of the diffraction pattern.

$$\hat{U}(P') = \frac{iU_o e^{i\omega t}}{\lambda r s} \iint_S e^{-ik(r+s)} dx_o dy_o \quad (2.2)$$

### 2.3 Fresnel Diffraction

By extending the earlier approximations, an equation may be derived which is useful in solving many types of diffraction problems. Let the distance from the source to the aperture be large enough that the wavefront generated by the source is essentially plane. If the coordinate system which is shown in Figure 2.02 is used, then the distances  $r$  and  $s$  may be expanded using the binomial theorem. After dropping all powers of  $x_o$  and  $y_o$  higher than the second, the following expressions for  $r$  and  $s$  are obtained.

$$r \approx r_o \left[ 1 + \frac{x_o^2 + y_o^2}{2r_o^2} - \frac{x_o x + y_o y}{r_o^2} - \frac{(x_o x + y_o y)^2}{2r_o^4} \right] \quad (2.3)$$

$$s \approx s_o \left[ 1 + \frac{x_o^2 + y_o^2}{2s_o^2} - \frac{x_o x' + y_o y'}{s_o^2} - \frac{(x_o x' + y_o y')^2}{2s_o^4} \right] \quad (2.4)$$

An amplitude approximation is now made by substituting  $1/r_o s_o$  for  $1/rs$  in the coefficient of the diffraction formula. The diffraction equation may be rewritten as

$$\hat{U}(P') = \frac{iU_o e^{i\omega t} e^{-ik(r_o + s_o)}}{\lambda r_o s_o} \iint_s e^{-ik[f(x_o, y_o)]} dx_o dy_o \quad (2.5)$$

where

$$f(x_o, y_o) = \left( -\frac{x_o x + y_o y}{r_o} - \frac{x_o x' + y_o y'}{s_o} \right) + \left[ \frac{x_o^2 + y_o^2}{2r_o} + \frac{x_o^2 + y_o^2}{2s_o} - \frac{(x_o x' + y_o y')^2}{2r_o^3} - \frac{(x_o x' + y_o y')^2}{2s_o^3} \right] \quad (2.6)$$

Physical processes which follow the assumptions made here are called Fresnel diffraction phenomena and are described by the above equation.

## 2.4 Fraunhofer Diffraction

The equation describing situations of Fresnel diffraction can be further simplified and still handle a large class of problems. If each of the distances  $r_o$  and  $s_o$  are very large compared to the maximum values of  $x_o$  and  $y_o$  in the plane of the aperture, then the bracketed terms in the Fresnel diffraction equation may be neglected. In addition to this, if the source is located on the  $z$ -axis so that  $x \sim 0$  and  $y \sim 0$  and the source is small enough compared to the aperture size to be considered a point source, then the first term in equation 2.6 may also be neglected. With these assumptions, the function  $f(x_o, y_o)$  is written as

$$f(x_o, y_o) = \left( -\frac{x_o x' + y_o y'}{s_o} \right) \quad (2.7)$$

and the Fresnel diffraction equation may be rewritten as

$$\hat{U}(P') = \frac{iU_o e^{i\omega t} e^{ik(r_o + s_o)}}{\lambda r_o s_o} \iint_S e^{i2\pi(k_x x_o + k_y y_o)} dx_o dy_o \quad (2.8)$$

where

$$k_x = x'/\lambda s_o$$

$$k_y = y'/\lambda s_o$$

This equation describes the cases when diffraction effects can be observed at distances which are considered large with respect to the aperture size. The type of diffraction effects observed under these conditions are termed Fraunhofer diffraction.

## 2.5 The Aperture Function

The diffraction equation contains an integration over the area of the aperture in which the effects of its size and shape are included into the determination of the diffraction pattern. It is often times convenient to define an aperture function which is introduced into the integral in the diffraction equation and contains all of this size and shape information. If this is done, the evaluation of the diffraction equation for different apertures becomes simplified. Let the aperture function be denoted by  $F(x_o, y_o)$ . The aperture function is dimensionless and when included into the above theory, the Fraunhofer diffraction equation becomes

$$\hat{U}(P') = \frac{iU_o e^{i\omega t} e^{ik(r_o + s_o)}}{\lambda r_o s_o} \iint_S F(x_o, y_o) e^{i2\pi(k_x x_o + k_y y_o)} dx_o dy_o \quad (2.9)$$

Since the surfaces which will be tested are rectangular, the first aperture shape which will be studied is the rectangular aperture. The significance of the rectangular aperture in this research is that the diffraction pattern produced by this aperture is the same that will be produced by a finite plate at rest.

## 2.6 The Rectangular Aperture

Consider a rectangular aperture of height  $2a$  and width  $2b$ . This aperture can be mathematically represented by the following

$$R_a(x_o) = 1 \quad \text{when } |x_o| \leq a$$

$$R_a(x_o) = 0 \quad \text{when } |x_o| > a$$

$$R_b(y_o) = 1 \quad \text{when } |y_o| \leq b$$

$$R_b(y_o) = 0 \quad \text{when } |y_o| > b$$

The aperture function  $F(x_o, y_o)$  is then just the product  $R_a(x_o)R_b(y_o)$ . When this aperture function is included in the Fraunhofer diffraction formula, the variables can be separated and the limits of integration can be changed from covering the area of the aperture to covering from negative infinity to positive infinity. The result is

$$\hat{U}(P') = \frac{iU_o e^{i\omega t} e^{ik(r_o + s_o)}}{\lambda r_o s_o} \int_{-\infty}^{\infty} \int_{-\infty}^{\infty} [R_a(x_o) e^{i2\pi k_x x_o}] [R_b(y_o) e^{i2\pi k_y y_o}] dx_o dy_o \quad (2.10)$$

$$= \frac{iU_o e^{i\omega t} e^{ik(r_o + s_o)}}{\lambda r_o s_o} \int_{-\infty}^{\infty} R_a(x_o) e^{i2\pi k_x x_o} dx_o \int_{-\infty}^{\infty} R_b(y_o) e^{i2\pi k_y y_o} dy_o \quad (2.11)$$

This expression is just the two dimensional fourier transform of the aperture function with the exception of the constants in front of the two integrals. The aperture function is a finite pulse whose fourier transform is the well known

sinc function,  $\text{sinc}(x) = \sin(x)/x$ , whose value at  $x=0$  is one and has zeros at integer multiples of  $\pi$ .

The One-Dimensional Sinc Function

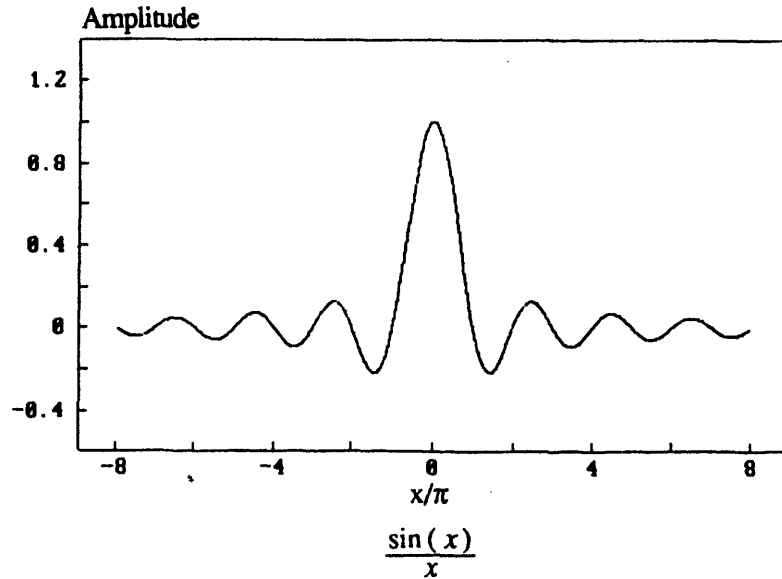


Figure 2.03 The one-dimensional sinc function.

The final expression for the diffraction pattern produced by a rectangular aperture, which is also the diffraction pattern produced by a flat finite plate at rest is

$$\hat{U}(P') = \frac{i 4abU_o e^{i\omega t} e^{ik(r_o + s_o)}}{\lambda r_o s_o} \text{sinc}(2\pi k_x a) \text{sinc}(2\pi k_y b) \quad (2.12)$$

## 2.7 The Comb Function

To continue with the theoretical development, it is useful to define a two-dimensional comb function. This function is obtained by first deriving a one-dimensional comb function and then extending the result to two-dimensions. The

comb function is just a sequence of  $N_x$  Dirac delta functions and is defined below. The variable  $L_x$  will represent the length of the test surface in the succeeding sections. The significance of shifting the delta functions in this way will also be shown later.

$$\Pi(x_o) = \sum_{q=1}^{N_x} \delta \left\{ \left[ \left( q - \frac{1}{2} \right) x_1 - \frac{L_x}{2} \right] - x_o \right\} \quad (2.13)$$

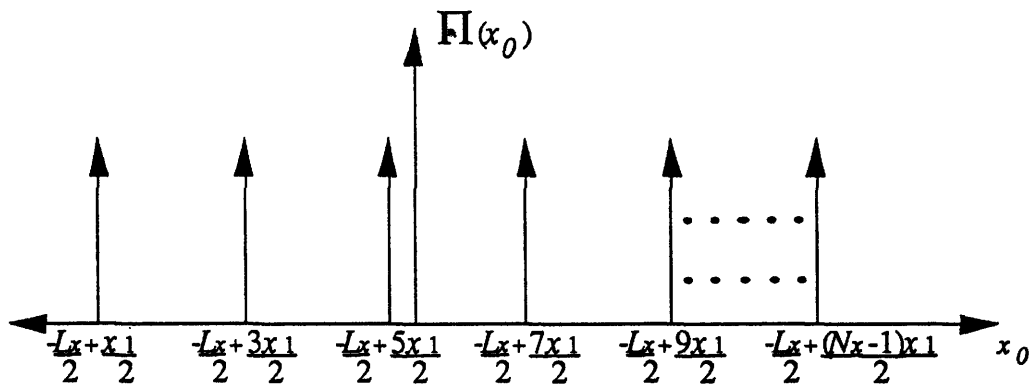


Figure 2.04 The one-dimensional comb function.

The fourier transform of the comb function is of interest to this discussion and is obtained by first looking at the transform of the shifted Dirac delta function. The fourier transform of the delta function at the origin is unity, but the fourier transform of a shifted delta function  $\delta[(x_1/2 - L_x/2) - x_o]$  is

$$\int_{-\infty}^{\infty} \delta \left[ \left( \frac{x_1}{2} - \frac{L_x}{2} \right) - x_o \right] e^{i 2\pi k_x x_o} dx_o = e^{-i 2\pi k_x \left( \frac{x_1}{2} - \frac{L_x}{2} \right)} \quad (2.14)$$



The desired fourier transform is then obtained from a summation over  $N_x$  delta functions which have been appropriately shifted. Let the double ended arrow signify the fourier transform in one direction and the inverse fourier transform in the other.

$$\prod(x_o) \leftrightarrow \int \sum_{q=1}^{N_x} \delta \left\{ \left[ \left( q - \frac{1}{2} \right) x_1 - \frac{L_x}{2} \right] - x_o \right\} dx_o \quad (2.15)$$

$$\leftrightarrow \sum_{q=1}^{N_x} e^{-i 2\pi k_x \left[ \left( q - \frac{1}{2} \right) x_1 - \frac{L_x}{2} \right]} \quad (2.16)$$

$$\prod(x_o) \leftrightarrow e^{i \pi k_x (L_x - N_x x_1)} \frac{\sin (N_x \pi k_x x_1)}{\sin (\pi k_x x_1)} \quad (2.17)$$

Section 2.8 will show that only even integer values of  $k_x x_1$  will be of interest to the work in this thesis. In this case the exponential term will turn out to be a complex constant of unit magnitude. To see how this transform behaves, it is advantageous to look at its magnitude and consider only even integer values of  $N_x k_x x_1$ . Then let two variables, denoted by  $\omega_1$  and  $\omega_2$ , be defined to group the arguments of the sine functions such that  $\omega_2 = N_x \omega_1$  and  $\omega_1 = k_x x_1$ . Upon doing so the comb function is written as

$$\prod(x_o) \leftrightarrow \frac{\sin (\omega_2 \pi)}{\sin (\omega_1 \pi)} \quad (2.18)$$

The numerator can be considered to have a higher effective frequency than the denominator. Its frequency is higher by a factor of  $N_x$  and will have a zero value  $N_x-1$  times in between the common zeros of the numerator and denominator. The ratio is an indeterminate form at a common zero. Application of L'Hopital's rule to this ratio will show that the ratio will approach  $N_x$  at a common zero. In addition to the  $N_x-1$  zeros, there will also be  $N_x-2$  maxima in between these zeros. The amplitude of these maxima will be much smaller than those which occur at common zeros. Thus the original ratio will reach a maximum value of  $N_x$  whenever the argument of the denominator is an integer multiple of  $\pi$  and will have substantially smaller amplitude elsewhere. A plot of this function is presented below.

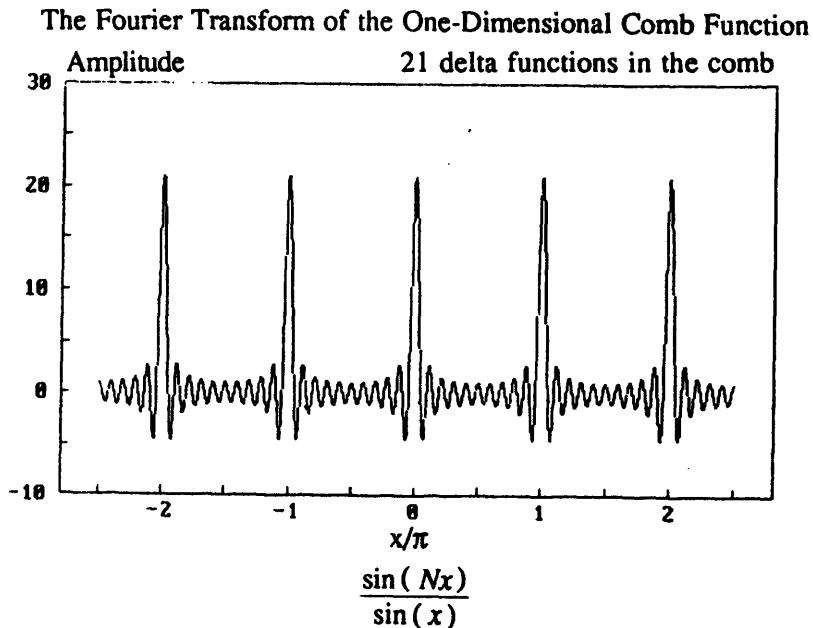


Figure 2.05 The fourier transform of the one-dimensional comb function.

In two dimensions, the comb function is simply a product of two terms similar to equation 2.17.

$$\prod(x_o, y_o) \leftrightarrow e^{i\pi[k_x(L_x - N_x x_1) + k_y(L_y - N_y y_1)]} \frac{\sin(N_x \pi k_x x_1)}{\sin(\pi k_x x_1)} \frac{\sin(N_y \pi k_y y_1)}{\sin(\pi k_y y_1)} \quad (2.19)$$

The bandwidth of the intensity peaks in the diffraction pattern are controlled by this function. The noise bandwidth of the intensity peaks is inversely related to the number of delta functions which make up the comb function. The noise bandwidth, which is denoted by  $\Delta$ , is given by the following expression.

$$\Delta = \frac{\pi^2}{N_x N_y} \quad (2.20)$$

## 2.8 The Phase Grating

The basic motivation of the work of this thesis lies in the theory of the phase grating. The diffraction effects discussed thus far are equally valid for a perfectly reflecting surface with finite dimensions as they are for an aperture, which is in essence a completely transmitting surface provided that the area surrounding the reflecting aperture completely absorbs the incident wave field. Therefore, the reflecting surface functions exactly as the aperture and the diffraction effects may be observed by looking at its reflected wave field. The phase grating is a surface which induces a sinusoidally varying phase shift across the incident wavefront.

Suppose the surface forming the grating is perfectly reflecting and has a surface profile which is given by

$$z(x_o, y_o) = z_x \sin\left(2\pi \frac{x_o}{\Lambda_x}\right) + z_y \sin\left(2\pi \frac{y_o}{\Lambda_y}\right) \quad (2.21)$$

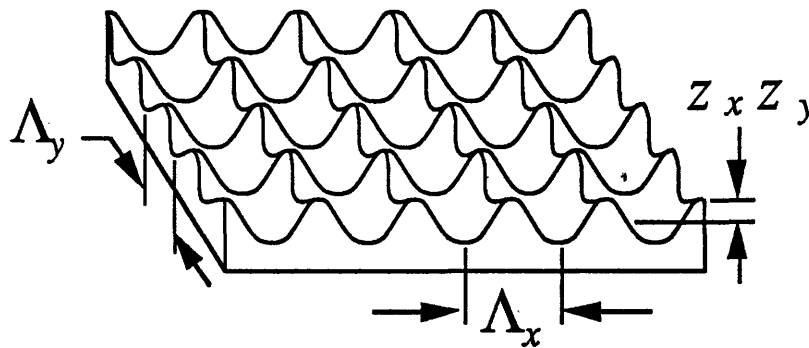


Figure 2.06 The two-dimensional phase grating.

$\Lambda_i$  is the wavelength of the sinusoidal surface displacement in the  $i^{th}$  direction and  $z_x z_y$  is the amplitude of this displacement. The amplitude  $z_x z_y$  is assumed to be small compared to the distance  $\Lambda_i$  between the surface wave crests. The amplitude is in fact so small that the maximum surface slope at any point is on the order of milliradians.

When a plane wave field is normally incident on this surface, there is a sinusoidal phase variation produced across the wavefront by the surface displacement. The surface slopes are so small, however, that the change in direction of the reflected waves on the diffraction pattern is negligible compared to the induced phase variation. The reflected wave will have a constant phase term

as well as a varying phase term. The constant phase term is not significant since it carries no information about the surface deformation. The varying phase term, which was induced by the surface profile, carries with the reflected wave all of the information needed to recreate this profile. The variable phase term is given by

$$\varphi(x_o, y_o) = k [2z(x_o, y_o)] \quad (2.22)$$

$$= \frac{2\pi}{\lambda} \left[ 2 z_x \sin\left(2\pi \frac{x_o}{\Lambda_x}\right) z_y \sin\left(2\pi \frac{y_o}{\Lambda_y}\right) \right] \quad (2.23)$$

$$\varphi(x_o, y_o) = \frac{4\pi}{\lambda} \left[ z_x z_y \sin\left(2\pi \frac{x_o}{\Lambda_x}\right) \sin\left(2\pi \frac{y_o}{\Lambda_y}\right) \right] \quad (2.24)$$

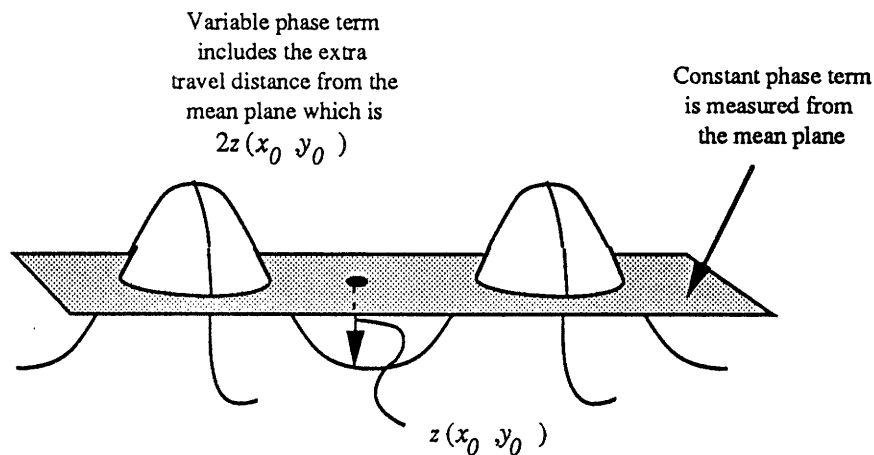


Figure 2.07 Geometric representation of the constant and variable phase terms.

The reflected wave then takes the following form (Notice the spatial dependence on  $x_o$  and  $y_o$ , which is transverse to the direction of propagation of the reflected wave.)

$$\hat{U}_o = \frac{U_o}{r_o} e^{i[\omega t - k\phi_o - \phi(x_o, y_o)]} \quad (2.25)$$

$$\hat{U}_o = \frac{U_o}{r_o} e^{i\left\{\omega t - k\phi_o - \frac{4\pi}{\lambda} \left[ z_x z_y \sin\left(2\pi \frac{x_o}{\Lambda_x}\right) \sin\left(2\pi \frac{y_o}{\Lambda_y}\right) \right]\right\}} \quad (2.26)$$

The comb function is a mathematical way of incorporating the effect of multiple periods of the surface wave into the discussion. If the effect of one complete period of the surface wave is represented by one of the delta functions in the comb, then the entire comb will represent multiple periods of the surface wave. The spacing of the delta functions in the comb must reflect the surface wavelength for this to be accurate. To accomplish this, a surface function, denoted by  $F_s(x_o, y_o)$ , is created to represent one period of the surface wave in each direction.

$$F_s(x_o, y_o) = \begin{cases} e^{-i \frac{4\pi}{\lambda} \left[ z_x z_y \sin\left(2\pi \frac{x_o}{\Lambda_x}\right) \sin\left(2\pi \frac{y_o}{\Lambda_y}\right) \right]} & \text{for } |x_o| \leq \frac{\Lambda_x}{2} \text{ and } |y_o| \leq \frac{\Lambda_y}{2} \\ 0 & \text{otherwise} \end{cases} \quad (2.27)$$

The convolution of a delta function, which has been shifted from the origin by an amount  $(x_1, y_1)$ , with the surface function will just reposition  $F_s(x_o, y_o)$  to have its center at  $(x_1, y_1)$ . If the distances between the delta functions in the two-

dimensional comb function,  $x_1$  and  $y_1$ , is set to equal the corresponding surface wavelengths,  $\Lambda_x$  and  $\Lambda_y$ , then the aperture function for the statically deflected sinusoidal surface is just the convolution of the comb function with the surface function.

$$G_p(x_o, y_o) = \prod(x_o, y_o) * F_s(x_o, y_o) \quad (2.28)$$

where  $G_p(x_o, y_o)$  is the phase grating aperture function  
 $*$  is the symbol for convolution

The number of complete surface waves present is now equal to  $N_x$  in the  $x$  direction and  $N_y$  in the  $y$  direction. The dimensions of the phase grating are  $N_x\Lambda_x$  by  $N_y\Lambda_y$ . All of the incident waves, which fall outside these boundaries, will not be reflected. The diffraction equation for the phase grating can now be written as

$$\hat{U}(P') = \frac{iU_o e^{i\omega t} e^{ik(r_o + s_o)}}{\lambda r_o s_o} \iint_s G_p(x_o, y_o) e^{i2\pi(k_x x_o + k_y y_o)} dx_o dy_o \quad (2.29)$$

The integral in the above equation is just the spatial fourier transform of the convolution of two functions represented by  $G_p(x_o, y_o)$ . The fourier transform of the convolution of two functions is just the product of the fourier transforms of the functions themselves. The fourier transform of the comb function has already been found in section 2.7 (See Equation 2.19). Therefore, to evaluate the

diffraction equation for the phase grating, the fourier transform of the surface function must be found. It is written as follows.

$$F_s(x_o, y_o) \leftrightarrow \int_{-\frac{\Lambda_y}{2}}^{\frac{\Lambda_y}{2}} \int_{-\frac{\Lambda_x}{2}}^{\frac{\Lambda_x}{2}} e^{-i \frac{4\pi}{\lambda} \left[ z_x z_y \sin\left(2\pi \frac{x_o}{\Lambda_x}\right) \sin\left(2\pi \frac{y_o}{\Lambda_y}\right) \right]} e^{i 2\pi (k_x x_o + k_y y_o)} dx_o dy_o \quad (2.30)$$

The integral can be simplified by making the following change of variables.

$$\begin{aligned} n &= k_x \Lambda_x & m &= k_y \Lambda_y \\ u &= \frac{2\pi}{\Lambda_x} x_o & dx_o &= \frac{\Lambda_x}{2\pi} du \\ t &= \frac{2\pi}{\Lambda_y} y_o & dy_o &= \frac{\Lambda_y}{2\pi} dt \end{aligned}$$

$$v = \frac{4\pi}{\lambda} z_x z_y \sin(t)$$

Thus

$$F_s(x_o, y_o) \leftrightarrow \frac{\Lambda_x \Lambda_y}{2\pi} \int_{-\pi}^{\pi} \left\{ \frac{1}{2\pi} \int_{-\pi}^{\pi} e^{i(nu - v \sin u)} du \right\} e^{imt} dt \quad (2.31)$$

If  $n$  is an integer, then the integral in the braces is the definition of a Bessel function of the first kind of order  $n$  and argument  $v$  [7]. The first five



integer orders of the Bessel function are shown in Figure 2.08. The reason only integer orders are of interest will be shown shortly.

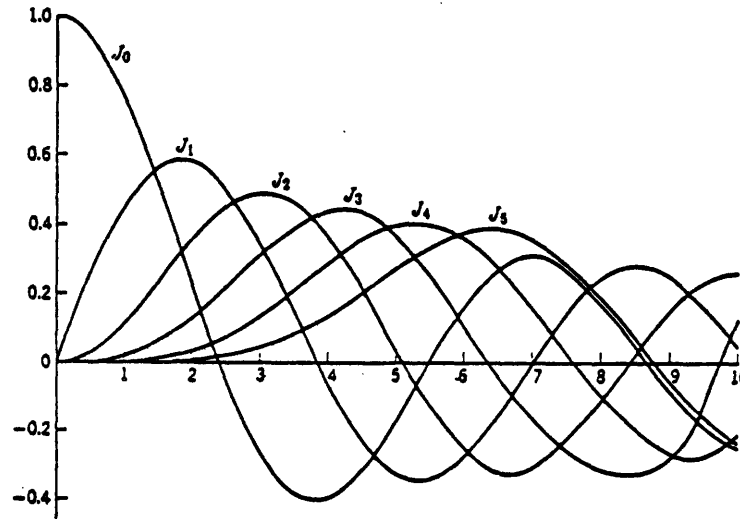


Figure 2.08 The first five integer orders of the Bessel function of the first kind.

If  $n$  is an integer, then the integral above is written as

$$F_s(x_o, y_o) \leftrightarrow \frac{\Lambda_x \Lambda_y}{2\pi} \int_{-\pi}^{\pi} J_n \left[ \frac{4\pi}{\lambda} z_x z_y \sin(t) \right] e^{imt} dt \quad (2.32)$$

The exponential term is now expanded to yield

$$F_s(x_o, y_o) \leftrightarrow \frac{\Lambda_x \Lambda_y}{2\pi} \int_{-\pi}^{\pi} J_n \left[ \frac{4\pi}{\lambda} z_x z_y \sin(t) \right] [\cos(mt) + i \sin(mt)] dt \quad (2.33)$$

This integral is now split up into two different parts. The first part of the integral contains even values of the integer  $n$ . The Bessel function is an even function when the order is even [7]. The sine function in the argument of the even Bessel function makes the Bessel function an even function of period  $2\pi$ . The integral over a full period of an even function times an odd function is equal to zero. The integral of an even function times another even function over a full period is equal to twice the value of the integral evaluated over a half period. Therefore, the only surviving terms are those containing an even order Bessel function times a cosine term. Similarly, the second part of the integral contains odd values of  $n$ . The Bessel function becomes an odd function when the order is odd [7]. The argument of the odd Bessel function causes it to be an odd function of period  $2\pi$ . The integral over a full period of an odd function times any other function is equal to zero. There are no surviving terms in the second part of the integral. The integral reduces to the following.

$$F_s(x_o, y_o) \leftrightarrow \frac{\Lambda_x \Lambda_y}{2\pi} 2 \int_0^\pi J_n \left[ \frac{4\pi}{\lambda} z_x z_y \sin(t) \right] \cos(mt) dt \quad (2.34)$$

$n = \text{even}$

This integral is found from [8] to be equal to

$$F_s(x_o, y_o) \leftrightarrow \Lambda_x \Lambda_y \cos\left(\frac{m\pi}{2}\right) J_{\frac{n-m}{2}}\left(\frac{2\pi}{\lambda} z_x z_y\right) J_{\frac{n+m}{2}}\left(\frac{2\pi}{\lambda} z_x z_y\right) \quad (2.35)$$

$n = \text{even}$

The cosine term causes only even values of  $m$  to be important. Therefore, the final result for the spatial fourier transform of the surface function for even integer values of  $n$  and  $m$  is

$$F_s(x_o, y_o) \leftrightarrow \Lambda_x \Lambda_y J_{\frac{n-m}{2}}\left(\frac{2\pi}{\lambda} z_x z_y\right) J_{\frac{n+m}{2}}\left(\frac{2\pi}{\lambda} z_x z_y\right) \quad (2.36)$$

$$n, m = \text{even}$$

Substitution for  $n$  and  $m$  in the above equation and for  $x_1$  and  $y_1$  in equation 2.19, yields the final expression describing the diffraction pattern produced by a two-dimensional statically deflected sinusoidal surface. The diffraction equation is

$$\hat{U}(P') = \frac{iU_o e^{i\omega t} e^{ik(r_o + s_o)}}{\lambda r_o s_o} \Lambda_x \Lambda_y J_{\frac{k_x \Lambda_x - k_y \Lambda_y}{2}}\left(\frac{2\pi}{\lambda} z_x z_y\right) J_{\frac{k_x \Lambda_x + k_y \Lambda_y}{2}}\left(\frac{2\pi}{\lambda} z_x z_y\right) \cdot \left\{ e^{i\pi[k_x L_x - k_y L_y]} \frac{\sin(N_x \pi k_x \Lambda_x)}{\sin(\pi k_x \Lambda_x)} \frac{\sin(N_y \pi k_y \Lambda_y)}{\sin(\pi k_y \Lambda_y)} \right\} \quad (2.37)$$

To understand how this equation behaves, it's advantageous to look again at the terms in the braces. The ratio of sines terms produce a main peak of interest whenever  $\pi k_x \Lambda_x$  and  $\pi k_y \Lambda_y$  are even integer multiples of  $\pi$ . The magnitudes of these peaks are  $N_x N_y$ . The secondary peaks in between these are much smaller in amplitude and may be neglected in the response. Therefore, the largest response occurs at the main peaks in the braced terms. The effects of the Bessel functions are important only at these main peaks in the braced terms, since in between these peaks the response is negligible.

The magnitude of the Bessel function is determined by both its argument and its order. Since the order of the Bessel functions are  $(k_x\Lambda_x - k_y\Lambda_y)/2$  and  $(k_x\Lambda_x + k_y\Lambda_y)/2$  and the main peaks in the response occur when  $k_x\Lambda_x$  and  $k_y\Lambda_y$  are even integers, it is seen that only even integer order Bessel functions are important in the diffraction equation. The argument of the integer order Bessel functions determines the distribution of radiant energy in the diffraction pattern. The amplitude of the surface deformation has been assumed to be very small. Therefore, the argument of the Bessel functions,  $v=2\pi z_x z_y/\lambda$ , is also small. It is seen from Figure 2.8 that the energy in the diffraction pattern is distributed between the different integer orders of the Bessel function with most of the energy in the zeroth and first order. This says that a sinusoidal surface displacement in the  $i^{th}$  direction will produce peaks in the diffraction pattern when  $\pi k_i \Lambda_i$  equals integer multiples of  $\pi$ . The magnitudes of these peaks are governed by the corresponding even integer order Bessel functions.

The magnitudes of the peaks in the diffraction pattern are related to the surface wave amplitudes through the Bessel functions. Experience has shown that the amplitude of a sound wave, which is reflected off of a vibrating surface, will fluctuate with time. Therefore, the surface wave amplitudes will be measured as described in section 2.10 and not through a measurement of the intensity in the diffraction pattern. The calculated values of the intensity are only important for overall signal to noise considerations.

The following plot shows a typical calculation of the distribution of energy in the diffraction pattern for a one-dimensional phase grating with surface amplitude equal to one tenth the wavelength of the incident wave field and wavelength equal to ten times the incident wavelength. The distance from the source and receiver to the phase grating is equal to four hundred incident wavelengths.

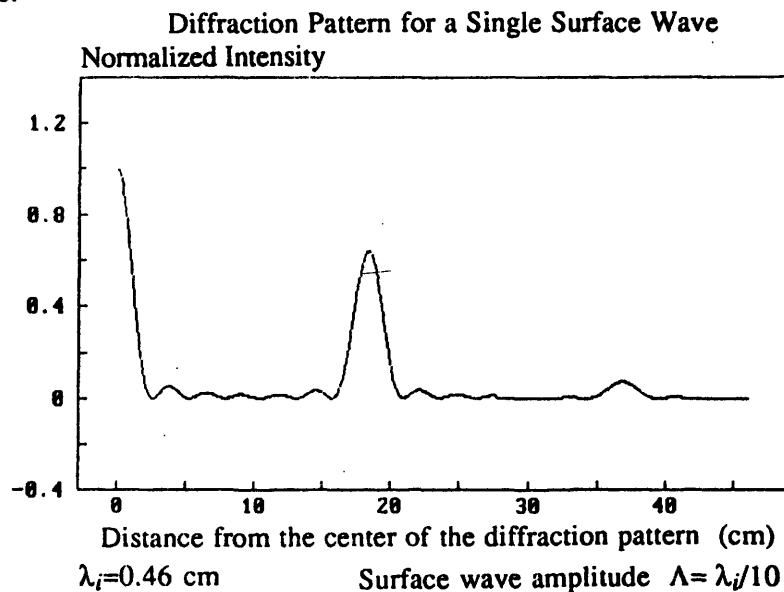


Figure 2.09 Calculated diffraction pattern for a one-dimensional phase grating with surface wavelength equal to  $10 \lambda_i$ . The distances  $r_o$  and  $s_o$  are equal to  $400 \lambda_i$ .

The plot is a direct measure of the wavenumber distribution of the phase grating provided that the argument of the Bessel functions are controlled so as to keep the amplitude of the first order much larger than the second. The wavenumber of the surface wave is directly related to the location of the intensity peak in the diffraction pattern.

## 2.9 The Complex Phase Grating

The theory of the phase grating can be extended to examine any complicated surface deformation through fourier analysis. Basically, any complex surface deformation can be fourier decomposed into its component spatial frequencies, each of which can act as a separate phase grating. The superposition of the diffraction patterns produced by each of these phase gratings will be the wavenumber distribution of the original surface. This is the case since each component phase grating produces a single peak in the diffraction pattern. The diffraction equation for a complex statically deformed finite surface now involves an integration over each surface wavelength present and becomes

$$\hat{U}(P) = \iint \frac{iU_o e^{i\omega t} e^{ik(r_o + s_o)}}{\lambda r_o s_o} \Lambda_x \Lambda_y J_{\frac{k_x \Lambda_x - k_y \Lambda_y}{2}} \left( \frac{2\pi}{\lambda} z_x z_y \right) J_{\frac{k_x \Lambda_x + k_y \Lambda_y}{2}} \left( \frac{2\pi}{\lambda} z_x z_y \right) \cdot \left\{ e^{i\pi[k_x L_x - k_y L_y]} \frac{\sin(N_x \pi k_x \Lambda_x)}{\sin(\pi k_x \Lambda_x)} \frac{\sin(N_y \pi k_y \Lambda_y)}{\sin(\pi k_y \Lambda_y)} \right\} d\Lambda_x d\Lambda_y \quad (2.38)$$

The following plots show calculations for the one-dimensional diffraction patterns produced by some proposed surface wavenumber distributions. These unrealistic shapes for the proposed wavenumber distributions were chosen to show the effect of the overlapping of the higher order Bessel functions of the individual phase gratings on the diffraction pattern. It is clear that the calculated diffraction patterns are direct reconstructions of these surface wavenumber distributions.

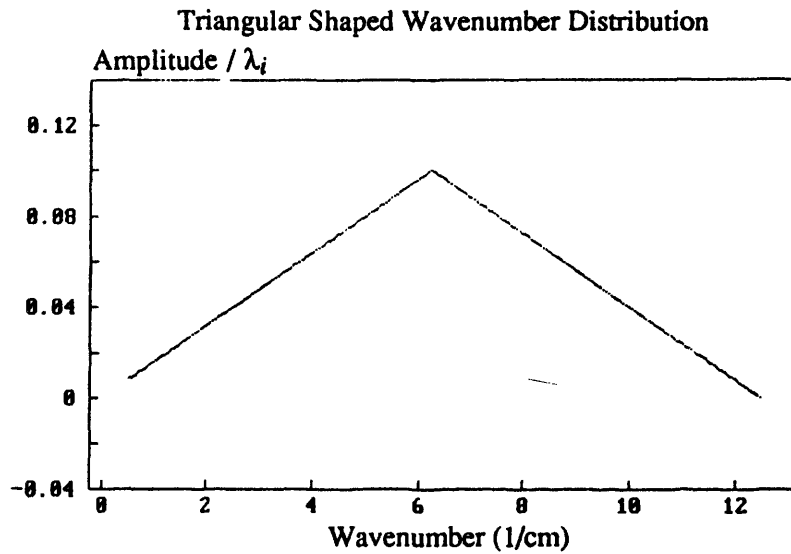
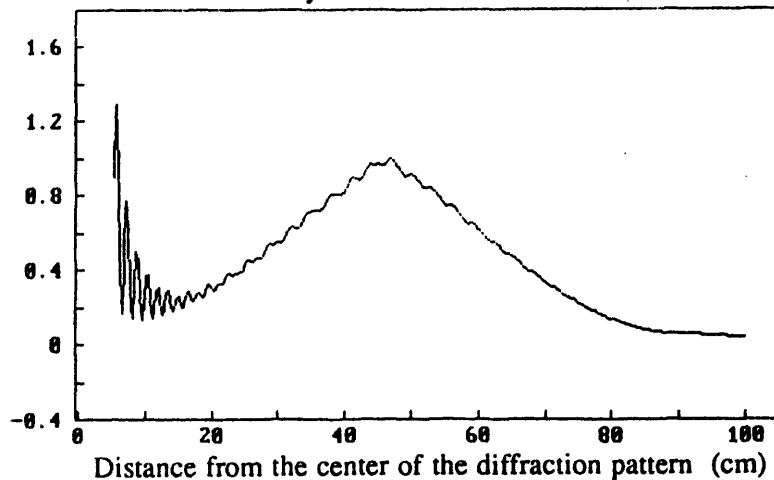


Figure 2.10 Example of a triangular shaped wavenumber distribution.

Diffraction Pattern for Triangular Shaped Wavenumber Distribution  
Normalized Intensity



$r_o, s_o = 1.0$  meter       $\lambda_i = 0.46$  cm

Figure 2.11 Calculation of the diffraction pattern for the triangular surface wavenumber distribution. This shows the effect of the overlapping of the higher order Bessel functions of the individual phase gratings, which form the wavenumber distribution.

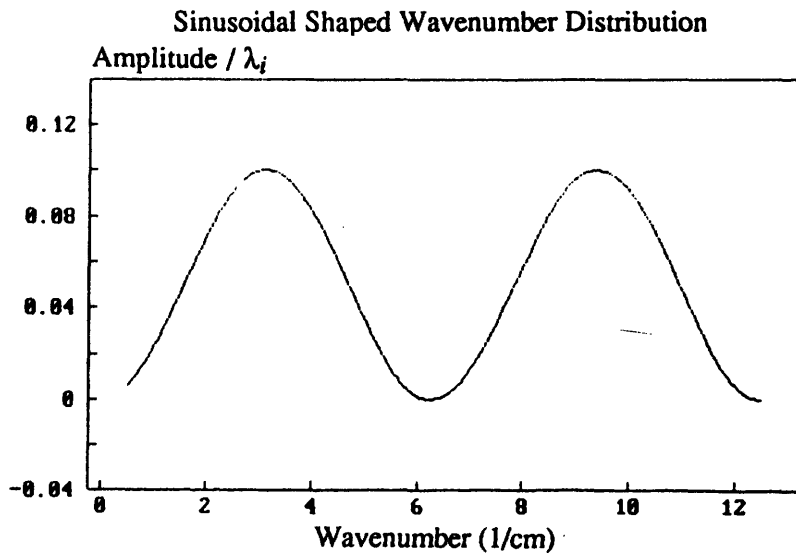
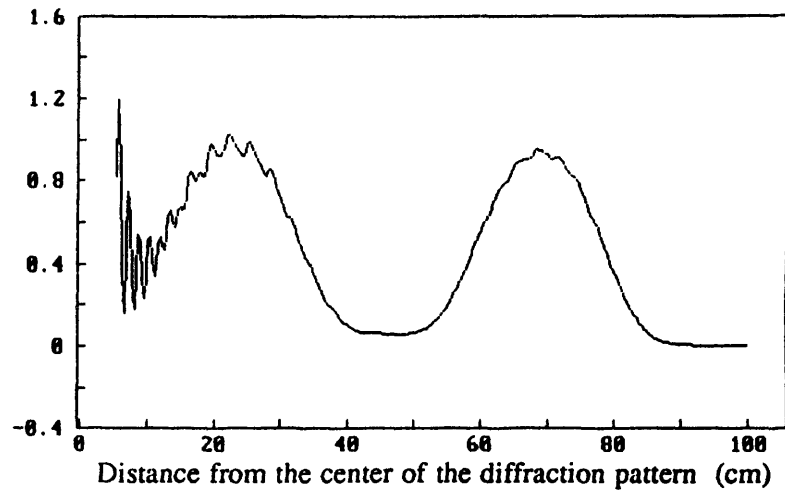


Figure 2.12 Example of a sinusoidal shaped wavenumber distribution.

**Diffraction Pattern for Sinusoidal Shaped Wavenumber Distribution**  
Normalized Intensity



$r_o, s_o = 1.0$  meter       $\lambda_i = 0.46$  cm

Figure 2.13 Calculation of the diffraction pattern for the sinusoidal surface wavenumber distribution. This shows the effect of the overlapping of the higher order Bessel functions of the individual phase gratings, which form the wavenumber distribution.



## **2.10 The Dynamic Complex Phase Grating**

The work in this thesis is aimed at measuring the wavenumber distribution for a vibrating surface. As the surface becomes dynamic, the reflected waves will be frequency modulated at the vibration frequencies due to the doppler shift imposed by the changing surface velocity. This allows the waves reaching the plane of the diffraction pattern to carry with them information about the surface vibration amplitudes without changing the diffraction effects. The amplitude of the vibration is directly related to the amount of frequency modulation in the reflected wave and is directly measured by measuring the amount of frequency modulation of the reflected wave. This places an additional restriction on the incident wavelength. The incident wavelength must be on the order of the vibration amplitude or smaller in order to produce a substantial amount of frequency modulation. A larger the amount of frequency modulation will produce a higher signal to noise ratio in the vibration amplitude measurement.

The complete wavenumber distribution can be measured in the following way. The location of a receiving sensor in the diffraction pattern determines the wavenumber of interest and its direction of travel on the surface. The spectrum of the frequency modulation of the reflected wave at this location provides the amplitudes of the frequencies of vibration of the wavenumber being measured. By scanning the diffraction pattern to cover all wavenumbers of interest, the complete wavenumber distribution for the vibrating surface can be measured directly.

### **3. Preliminary Experiments**

#### **3.1 Determination of the Type of Incident Wave**

To verify the theory and test this method of measurement, the type of incident wave field to use had to be determined. The theory brought about the following considerations.

- 1) There must be a relatively easy way in which to separate the incident and reflected wave field.
- 2) The wavelength of the incident wave field must be on the order of magnitude of the vibration amplitude or smaller.
- 3) The incident wave field must strike the vibrating surface with plane rather than spherical wavefronts.
- 4) The source size must be much smaller than the dimensions of the surface under investigation.
- 5) The appropriate transducers to send and receive the wave field as well as a means to frequency demodulate the reflected wave must be readily acquired.

Laser light was chosen to be the incident wave field since it met each of these requirements quite well. A coherent beam of single frequency light could be easily created and expanded to the appropriate beam width. The light beam would automatically have plane wavefronts and travel long distances. The incident and

reflected waves could be easily separated with a beamsplitter and the demodulation could be performed with two Bragg cells and a signal analyser.

### 3.2 The Prototype Laser Experiment

Once the choice of using laser light had been made, the following system was designed and fabricated.

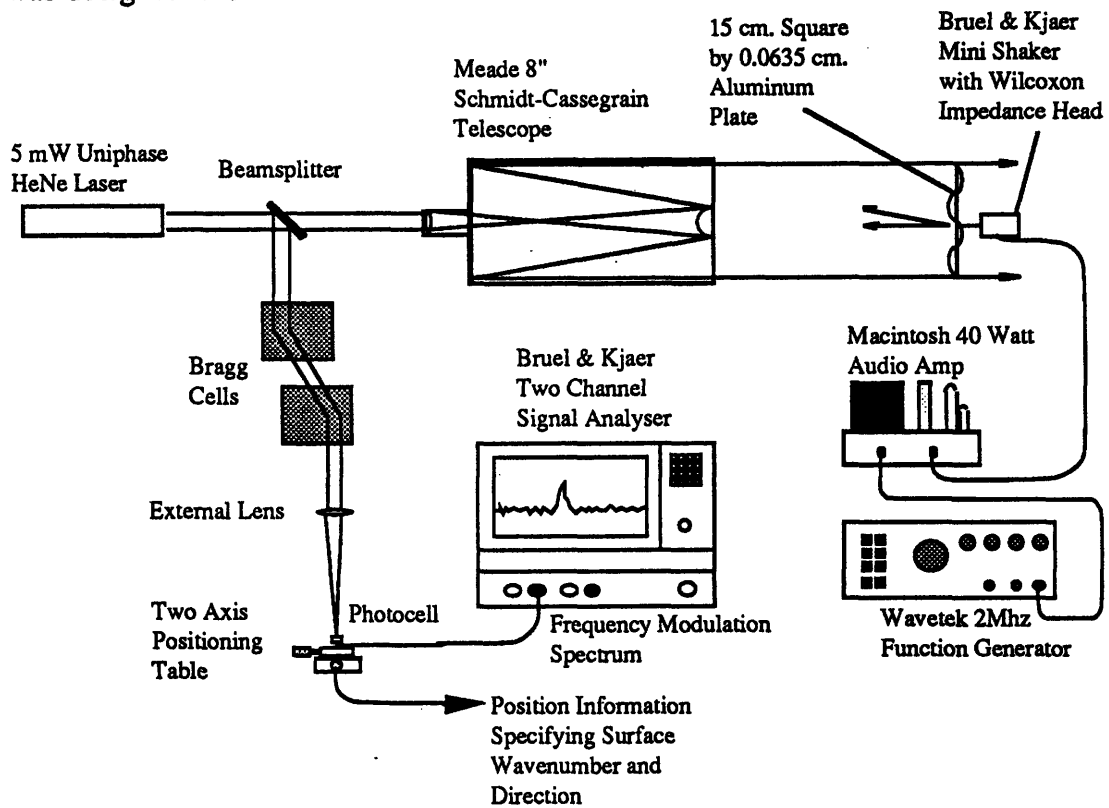


Figure 3.01 Schematic of the prototype laser experiment.

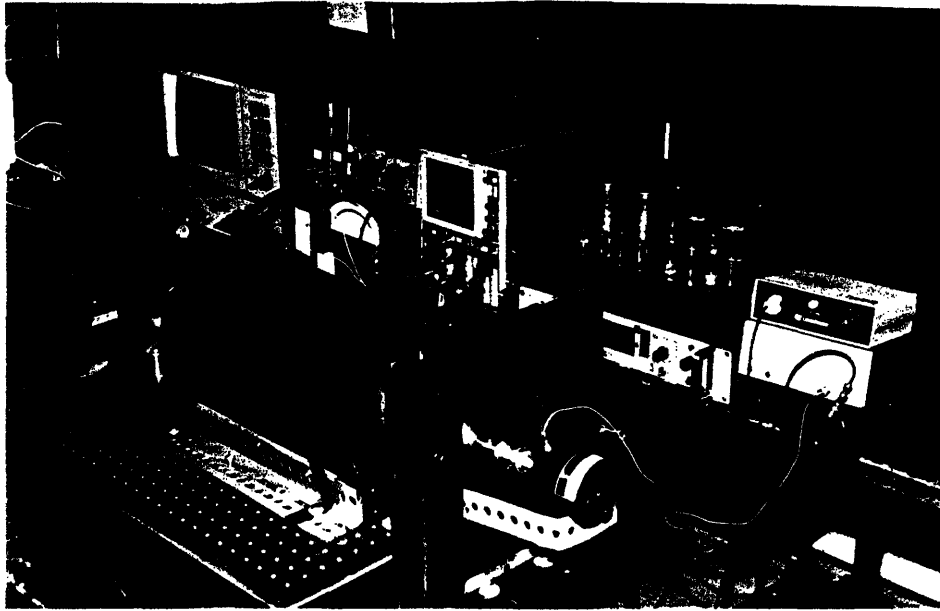


Figure 3.02 Photograph of the prototype laser experiment.

A 5 milliwatt Uniphase HeNe laser provides the coherent beam of incident light. This light beam travels through a beamsplitter and into the eyepiece of a Meade LX5 eight inch Schmidt-Cassegrain telescope, which expands the beam to a diameter of eight inches. The expanded beam of light reflects off the vibrating plate and travels back through the telescope, where it is reduced to its original beam width, and is turned ninety degrees by the beamsplitter. Two oppositely acting Bragg cells separate the frequency modulated part of the beam of light from the light at the carrier frequency. An external lens is positioned after the beamsplitter to bring the image of the diffraction pattern down to a focus. The diffraction pattern occurs in the focal plane of the external lens. A photodetector is used to measure the light in the diffraction pattern. The modulation signal from the photodetector is fed into a Bruel & Kjaer Dual Channel Signal Analyser Type 2032 to display the vibration frequency spectrum.

### 3.3 Preliminary Findings

Initial tests were carried out with this system and encountered the following problem was encountered. The amount of light which arrived at the plane of the diffraction pattern was of too low a level to measure. The reason for this was found to be due to two effects. First, the incident wavelength of the laser light was so small that the measurement was being effected by the surface irregularities on the plate. When the plate is at rest, the diffraction pattern should be that formed by a rectangular aperture. Any reflected light should arrive at the diffraction pattern with no frequency modulation and should form a two dimensional sinc function as stated in the theory. Instead of this, the light in the diffraction pattern was a low level spatially broad band illumination. This diffraction pattern turned out to be the wavenumber distribution of the random surface irregularities on the plate. In other words, the non-vibrating plate didn't appear flat to the incident wave field. Second, since the spatial frequency content of the surface irregularities was more or less white, most of the incident light intensity was reflected at angles which were too great to successfully make it back through the telescope and beamsplitter and to the diffraction pattern, and was therefore lost. When the surface was vibrated and sinusoidal disturbances were superimposed over these surface irregularities, the signals in the diffraction pattern due to the vibration were much lower in intensity than those due to the surface irregularities. Thus, the signal (imposed vibration wavenumber distribution) to noise (wavenumber distribution of the surface irregularities of the plate) was too low to feasibly make the desired measurement.

The solution to this problem was to make the static plate appear flat to the incident wave field. This could be done in two ways. Either a plate, which was flat to within a wavelength of HeNe laser light, had to be used or the incident wave field needed to have a longer wavelength. The latter solution was chosen so that this method could be used on surfaces of interest for structural acoustics experiments.

In support of this choice, it was also noted that the use of the laser caused the measurement system to be very sensitive to alignment. The laser system was so sensitive that the entire experiment had to be performed on an optical table. This would make field measurements with the laser system unfeasible.

## **4. Final Experiments**

### **4.1 Choosing the Alternate Wave Field**

The added requirement of enlarging the incident wavelength brought about an investigation into both infrared and ultrasonic wave fields. Infrared has the advantage of being able to travel long distances without much attenuation, but has the drawback of requiring some very expensive hardware. It also didn't appear possible to generate infrared waves of sufficient wavelength to avoid the same types of problems encountered with the laser light. The use of sound waves seemed promising for the following reasons.

- 1) The incident wavelength could be easily adjusted to meet the particular vibration amplitude and surface roughness conditions.
- 2) The sound waves would travel in water as well as in air.
- 3) The longer incident wavelength would cause the measurement system to be less sensitive to alignment.
- 4) The sensors required to generate and detect high frequency sound waves were relatively inexpensive.

Despite the expected problems of large amounts of attenuation with distance traveled and the separation of the incident and reflected wave fields, ultrasonic sound waves were chosen as the incident wave field.

## 4.2 Initial Ultrasonic Transducer Choice

The appropriate transducers to send and receive the sound waves must meet each of the requirements outlined in Chapter 3. The main requirement of the theory is that the incident wavefronts are plane. This demands that the source be a sufficient distance from the vibrating plate to ensure a large radius of curvature of the spherical wave emanating from the point source. A forty kilohertz sound wave traveling in air a distance of five meters will be attenuated about thirty-five decibels. When the sound wave is reflected off of the vibrating surface, there is an additional attenuation of between one to three decibels. The high amount of attenuation of the amplitude of the sound wave at the ultrasonic frequencies was the most important consideration in the choice of transducers. Therefore, the ideal source is one which would transmit an ultrasonic sound wave at the desired frequency a long enough distance to make the wavefronts appear plane. The ideal receiver is one that is extremely sensitive, and has a flat response over a frequency band twice as wide as the vibration frequencies of interest. The operating frequency of the transducers must also be high enough to be substantially modulated by the small vibration amplitudes. A tradeoff developed between the incident wavelength (operating frequency) and the distance of travel of the sound wave.

The chosen designs were resonant transducers produced by Massa Products of Hingham, Mass. Transducers operating at frequencies of 23, 31, 40, 75, 150, and 215 kilohertz were offered. The TR-89/B Type 40 (40khz) and E-152/75



(75khz) transducers were chosen since they were the transducers which generated the highest frequency sound wave capable of traveling a great enough distance to approximate plane waves incident on the plate and still be able to travel back to the plane of the diffraction pattern. The higher frequency transducers were much more desirable with respect to generating a substantial frequency modulation for a given vibration amplitude, but had the disadvantage of a short travel distance in air. The specifications for the Massa Products transducers are included in Appendix A along with some calculations indicating how close to plane the incident wavefronts would be on the vibrating plate given the maximum distance of travel of the generated sound wave.

To verify that these transducers produce a substantial output, their sound power output was measured at a distance of one foot and compared to the sound power output of a stereo tweeter. This test was performed to find out how much better these resonant transducers are than more conventional design. The tweeter's frequency response curve is located in Appendix A. The results of the tests are displayed below.

Transducer	SPL (dB re 20 microPa)	
	40 Khz	75 Khz
TR-89	115.9	-----
E150/75	-----	95.2
Tweeter	120.1	100.8

Table 4.1 Maximum sound power output of chosen sensors at a distance of one foot.

Although the sound power produced with the tweeter is slightly higher than that produced with the chosen transducers, it was seen that the amplitude of the generated wave varied with time. This is due to overdriving the tweeter to produce this high output. In this light, the chosen transducers were more desirable than the conventional stereo tweeter in generating the high frequency wave field.

### 4.3 The Ultrasonic Measurement System

The ultrasonic measurement system was modeled after the prototype laser system and built as shown below in Figures 4.01 and 4.02.

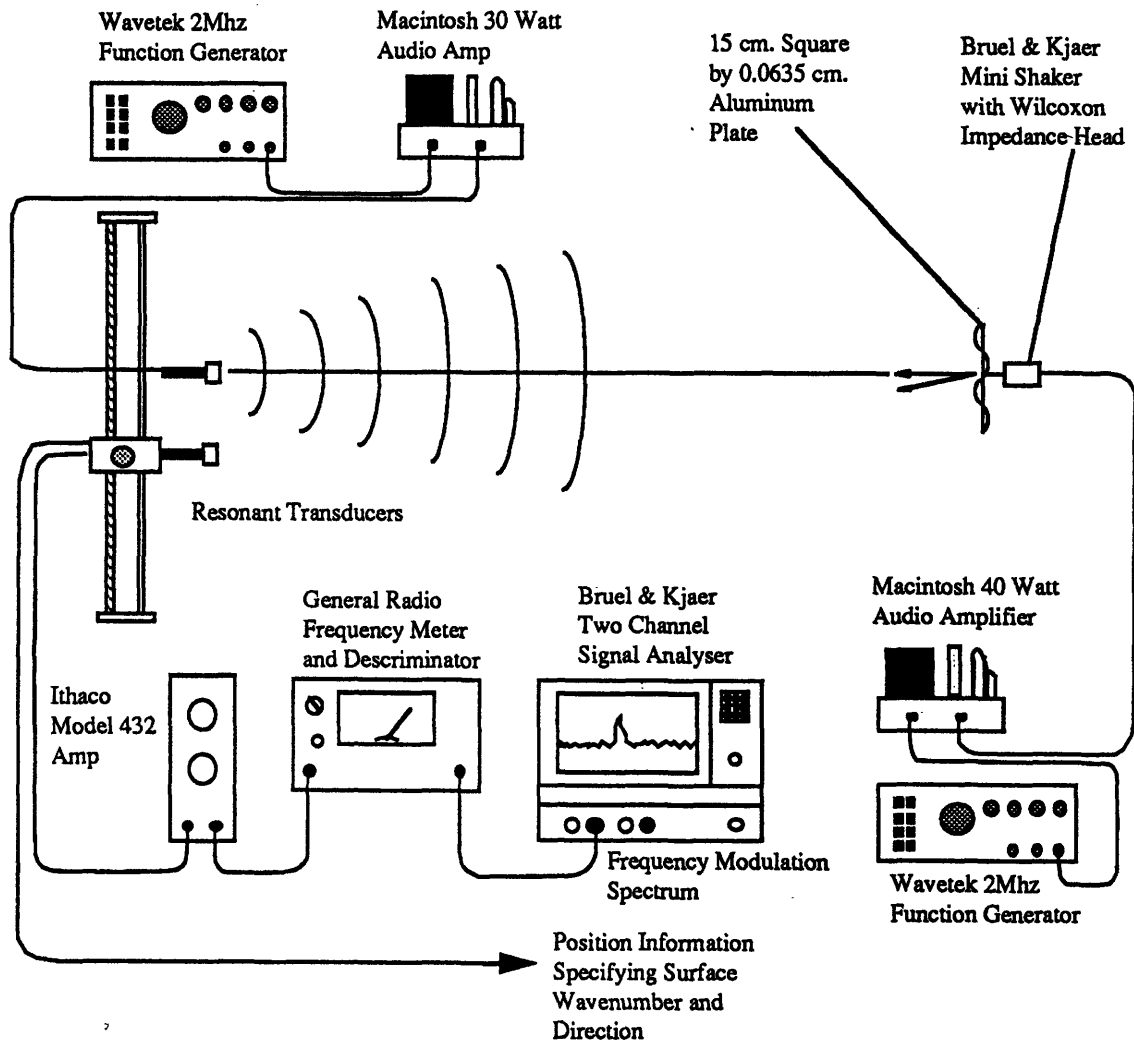


Figure 4.01 Schematic of the ultrasonic measurement system.



Figure 4.02 Photograph of the ultrasonic measurement system.

The incident wave field was generated by driving the transducer at its resonant frequency with a Wavetek 2Mhz Function Generator Model 20 and a Macintosh 30 Watt Audio Amplifier. A horn, which reduces the cone angle of the sound waves leaving the source, was designed and built to increase the overall signal to noise ratio. The horn makes the beam width of the incident waves just large enough to completely cover the plate but keeps it from becoming so much bigger than the plate that a substantial portion of the incident intensity is lost. The separation of the incident wave field from the reflected wave field was accomplished by scanning with the receiver in the plane of the source parallel to the plane of the vibrating plate. This method allows the entire diffraction pattern to be measured except for the point where the source is located. The receiving response of the transducers is broadened to a band around the transmitting

frequency by placing the transducer in parallel with an inductor and a resistor of the appropriate values (See Appendix A).

The signal received in the diffraction pattern is amplified with an Ithaco Model 432 amplifier and then high pass filtered with a Krohn-Hite Model 3550 filter to pass only the modulated carrier signal. The frequency modulated signal is then fed into a General Radio Frequency Meter and Discriminator Type 1142-A. This device generates a pulse train of constant amplitude and duration with a frequency that follows the input frequency. This signal has a average value that varies directly with the frequency modulation of the input signal. This signal is put into the Bruel and Kjaer Dual Channel Signal Analyzer Type 2032. The analyzer automatically low pass filters the signal below the carrier frequency leaving only the varying DC component. The frequency spectrum of this signal is displayed on the screen and is the spectrum of the modulation component in the received signal. Therefore, this spectrum is a measure of the vibration amplitude and frequency associated with the particular wavenumber under investigation as given by the position of the receiver.

#### **4.4 The Test Surface**

To verify the theory, a surface vibrating with a known wavenumber distribution is required. This suggests exciting a resonant mode of a finite plate that would be relatively easy to detect in the diffraction pattern. The surface which was chosen was a fifteen centimeter square by 0.0635 centimeter thick

aluminum plate, which was clamped at its boundaries and driven at its centerpoint. The reasons for this choice are the following. The boundary conditions used needed to be as uniform as possible around the perimeter of the plate to set up simple symmetrical mode shapes. Experimentally, clamped-clamped boundary conditions are most easily generated. The plate was made out of thin aluminum to increase the velocity of vibration as much as possible while avoiding membrane like vibration of the plate. The greater the vibration velocity, the greater the amount of frequency modulation in the reflected sound waves. The drive point was chosen to be at the center of the plate to force any spurious drive point effects to retain cross-axis symmetry.

The plate was excited with a Bruel and Kjaer Mini Shaker Type 4810. The shaker was driven with a Wavetek 2Mhz Function Generator Model 20 and a Macintosh 40 Watt Audio Amplifier. A Wilcoxon Research Model Z-602 impedance head was used to make the drive point transfer function measurements. The test rig, which supports the plate, was designed so that the entire plate could be tilted at any angle relative to the normally incident plane wavefronts. This feature aided in accurately aligning the measurement system. Acoustic foam surrounded the plate to absorb the sound waves which are incident on the supporting surfaces.

## 4.5 Generating and Measuring a Mode of Vibration

Figure 4.03 displays a drive point conductance measurement, which was made with the impedance head, and shows the resonant frequencies of the plate.

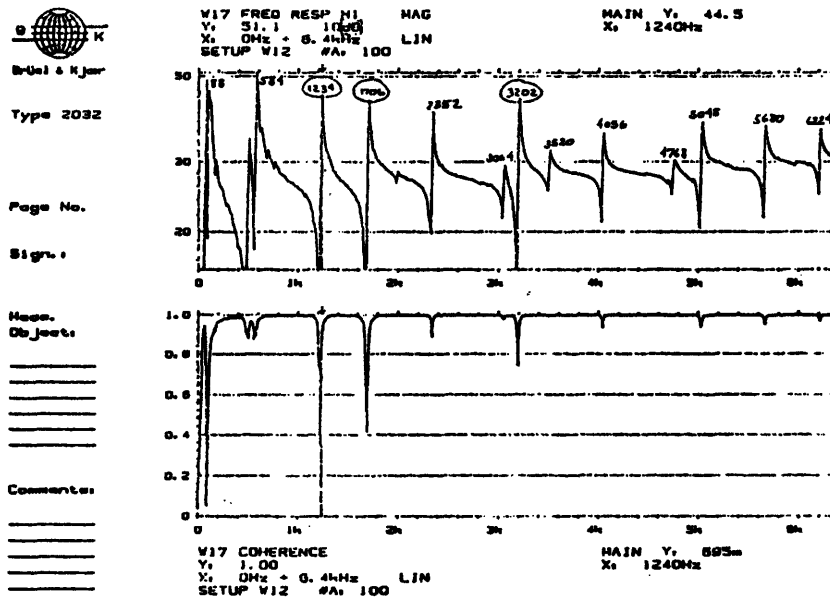


Figure 4.03 Drive point conductance measurement for the plate under test.

Given the distance of travel and frequency of travel of the sound waves supplied by the chosen transducers, it was determined that the higher order modes of vibration would be most easily detected in the diffraction pattern. These modes cause the peaks in the diffraction pattern to be spread further apart than those due to the lower modes. The bandwidth of the peaks is inversely related to the number of full surface waves on the plate. Since the higher modes contain more full surface waves, the wavenumber resolution of the measurement system is greater for these modes of vibration. The theory predicts a peak in intensity to be generated in the center of the diffraction pattern, which can be interpreted as the

DC level of the surface wavenumber distribution. This center peak is usually the largest in the diffraction pattern, since its amplitude is controlled by the zeroth order Bessel function. Therefore, it is desirable to set up a higher order mode of vibration so that the peaks due to the surface waves are as narrow as possible and are not overshadowed by the large center peak. In addition to this, the peaks must be spread apart at least as much as twice the transducer size. With this in mind, three of the cleanest and largest amplitude resonant frequencies were chosen for testing. These frequencies were 1234 hz, 1706 hz, and 3202 hz.

Once the choice of resonant modes had been made, the plate was excited at these frequencies and the resultant horizontal mode shapes were measured by scanning across the surface with a Mechanical Technology Incorporated Model KD-45A Fotonic Sensor. The fotonic sensor measures the maximum vibration amplitude at each point. The phase of the vibration at each point with respect to the input force was also recorded to help reconstruct the mode shape. The calibration curve and specifications for the fotonic sensor are presented in Appendix B. The experimental setup is shown in Figures 4.04 and 4.05.



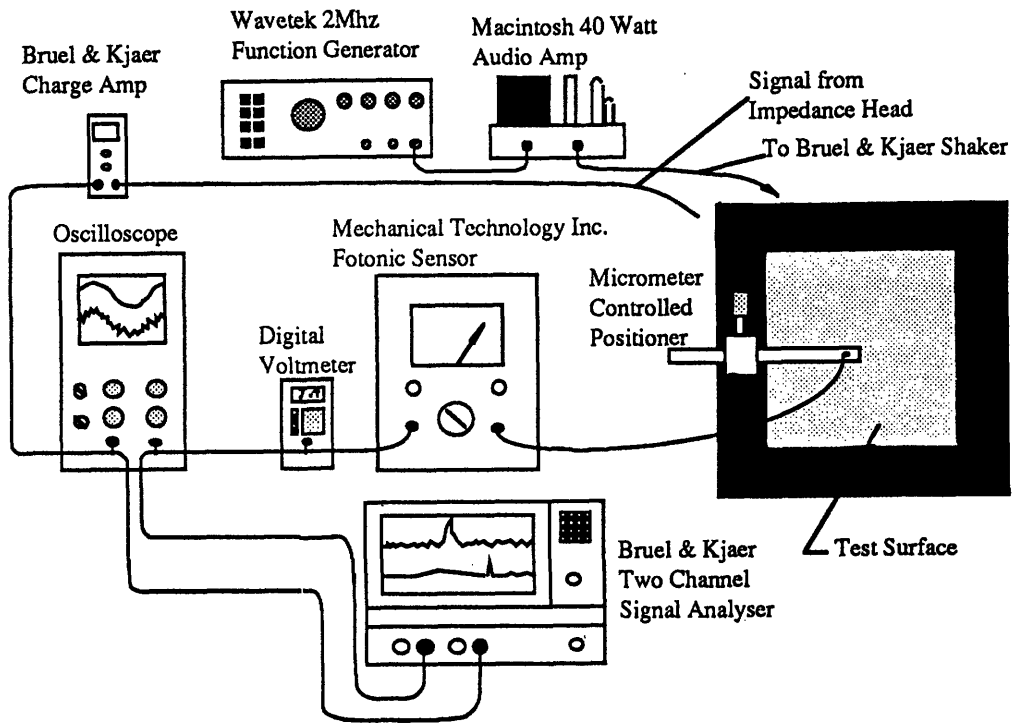


Figure 4.04 Schematic of the mode shape measurement system.

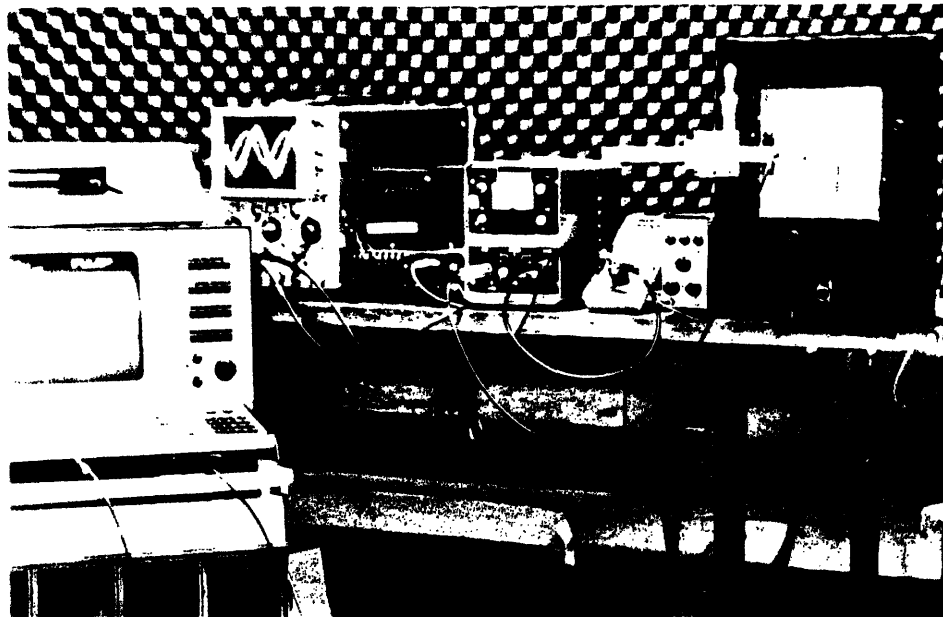


Figure 4.05 Photograph of the mode shape measurement system.

Since the diffraction pattern was to be scanned in the horizontal direction, three horizontal scans of 32 points each were made across the plate at each frequency. The horizontal mode shapes were defined quite well with the three scans. The results of these measurements are displayed pictorially below. The actual data, which was taken to yield these pictures of the generated mode shapes, is included in Appendix C.

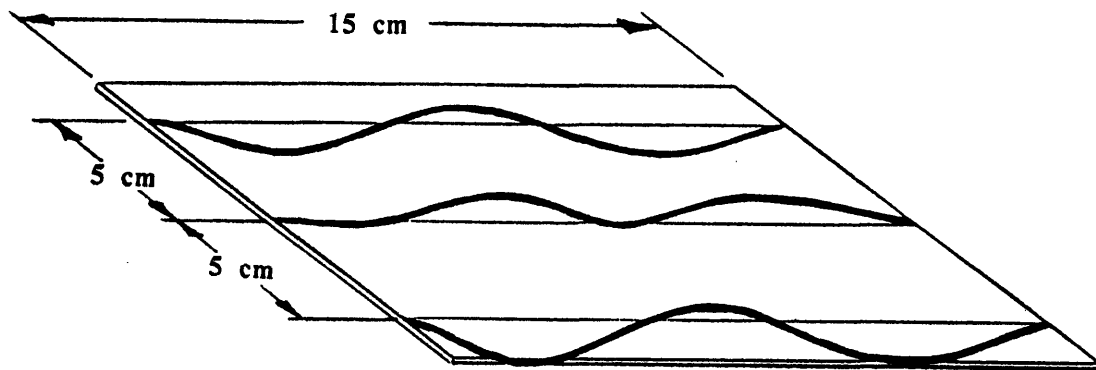


Figure 4.06 Measured horizontal mode shape of the test surface at a vibration frequency of 1234 hz.

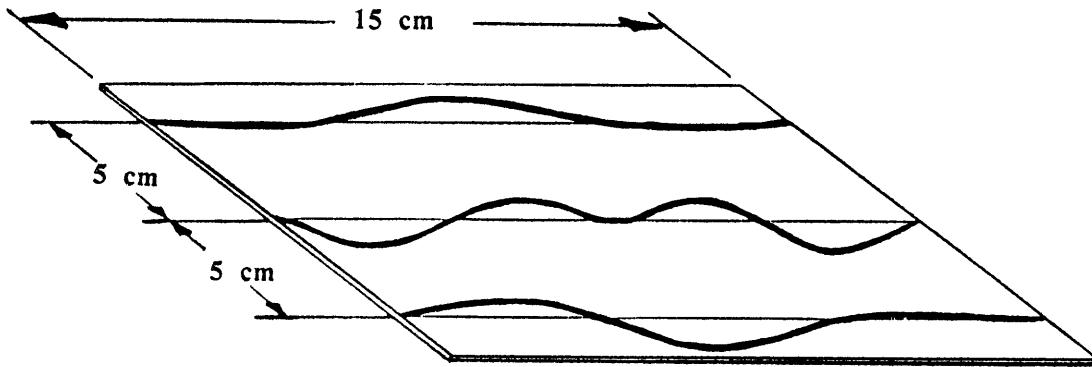


Figure 4.07 Measured horizontal mode shape of the test surface at a vibration frequency of 1706 hz.

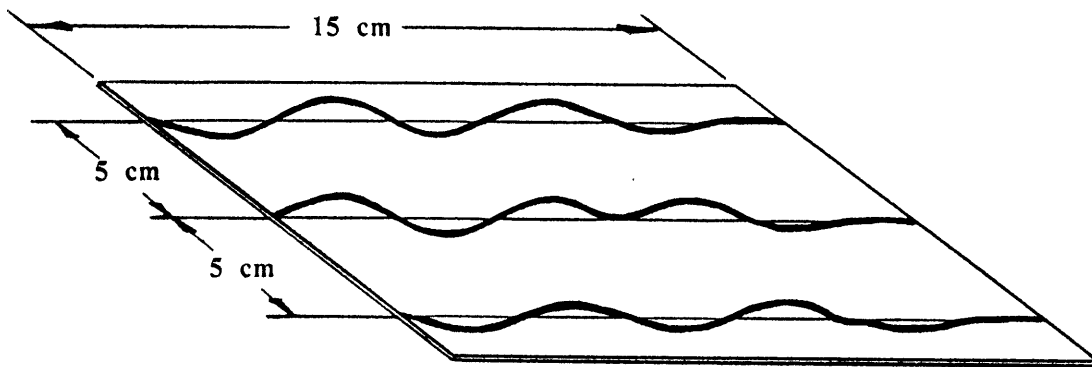


Figure 4.08 Measured horizontal mode shape of the test surface at a vibration frequency of 3202 hz.

From these pictures, it appears that the third fundamental mode of vibration was set up in the horizontal direction at 1234 hz and 1706 hz input frequencies. At 3202 hz the sixth fundamental mode of vibration was present in the horizontal direction. The drive point effects can be seen only along the plate centerline and are damped out as the scans were away from the plate centerpoint. These modes correspond to spatial wavelengths of 10 cm and 5 cm respectively. The bending wavelengths associated with the input frequencies were calculated with the following equation and are displayed in Table 4.2.

$$\lambda_b = 2\pi \sqrt{\frac{\kappa c_l}{\omega_v}}$$

where  $\lambda_b$  is the bending wavelength  
 $\kappa$  is the radius of gyration of the plate  
 $c_l$  is the longitudinal wave speed in the plate  
 $\omega_v$  is the vibration frequency

Vibration Frequency (hz)	Bending Wavelength (cm)
1234	6.9
1706	5.8
3202	4.3

Table 4.2 Bending wavelengths associated with each input frequency.

The measured mode shapes are oblique. That is, the bending waves are not traveling horizontally or vertically on the plate. The scans are measuring the horizontal component of the bending waves traveling on the plate.

The expected diffraction pattern produced by the horizontal modes of vibration were predicted with a computer program, which is presented in Appendix D. The computer program first calculates the wavenumber distribution for a specified horizontal mode of vibration of the finite plate and then calculates the intensity in the resulting diffraction pattern. The expected amplitude of the wavenumber distribution is found from the mode shape measurements with the fonic sensor. The average maximum amplitude of the horizontal mode shape was used to scale the predicted diffraction patterns to the appropriate displacement magnitude. Plots of the calculated wavenumber distributions corresponding to the horizontal mode shape measurements and their expected diffraction patterns are shown in Figures 4.09 through 4.16.

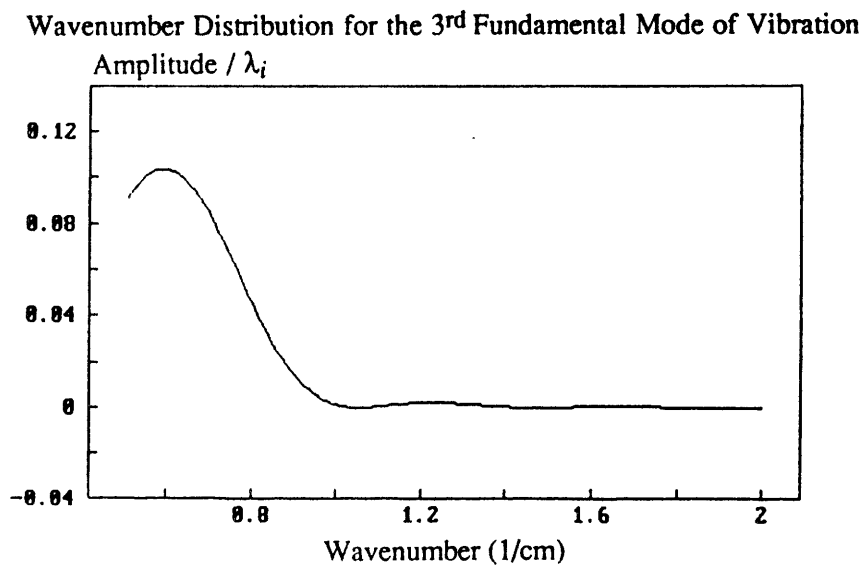


Figure 4.09 Calculated wavenumber distribution for the third fundamental mode of vibration of the test surface.

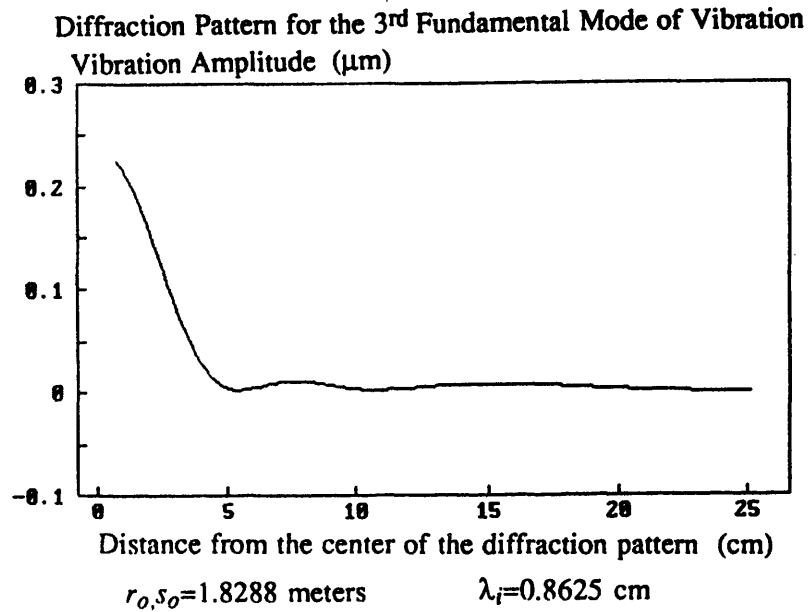


Figure 4.10 Calculated diffraction pattern for the third fundamental mode of vibration using a 40 khz sound wave.

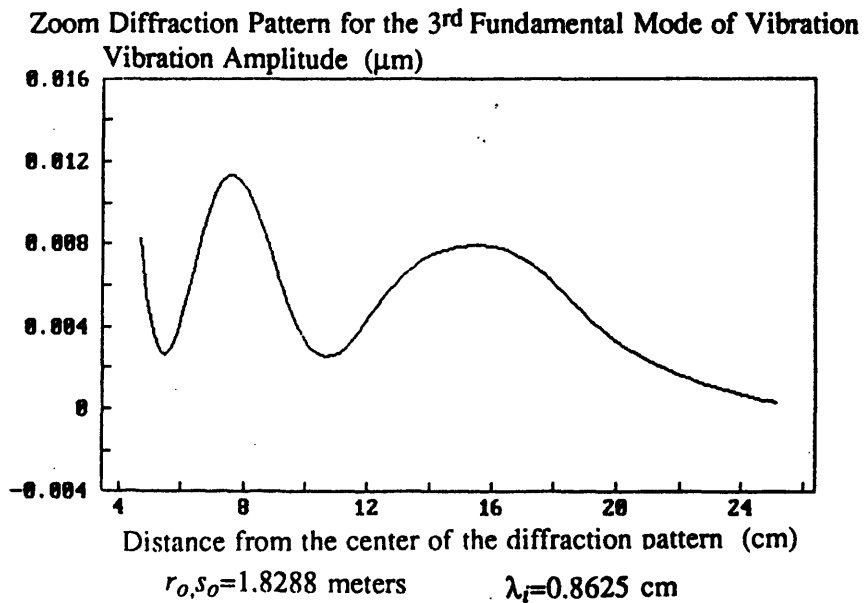


Figure 4.11 Zoom view of the calculated diffraction pattern for the third fundamental mode of vibration using a 40 khz sound wave.

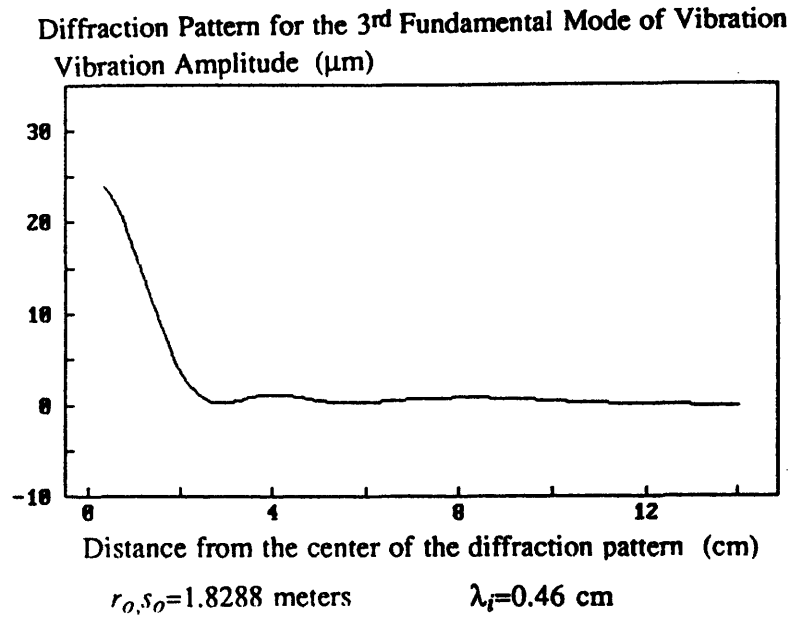


Figure 4.12 Calculated diffraction pattern for the third fundamental mode of vibration using a 75 khz sound wave.

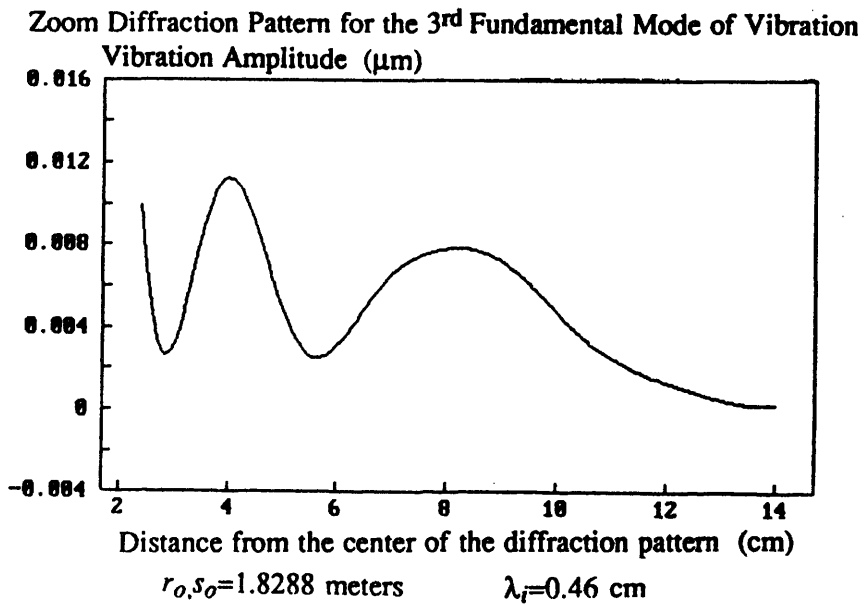


Figure 4.13 Zoom view of the calculated diffraction pattern for the third fundamental mode of vibration using a 75 khz sound wave.

Wavenumber Distribution for the 6<sup>th</sup> Fundamental Mode of Vibration

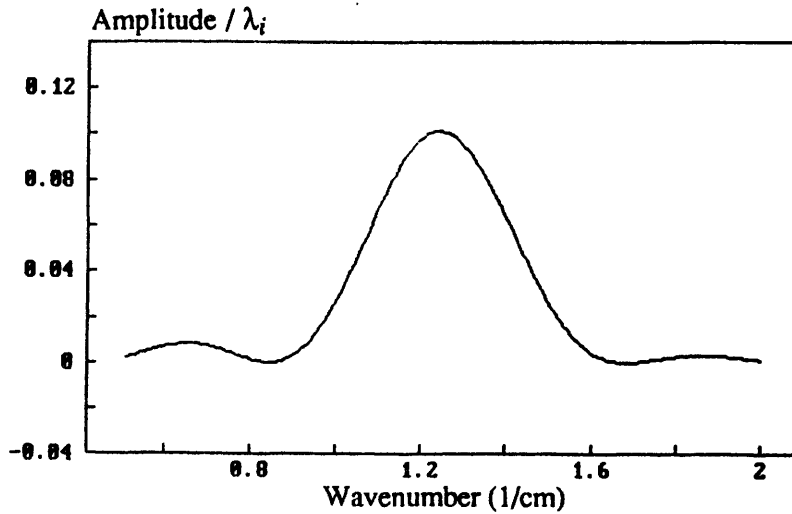


Figure 4.14 Calculated wavenumber distribution for the sixth fundamental mode of vibration of the test surface.

Diffraction Pattern for the 6<sup>th</sup> Fundamental Mode of Vibration

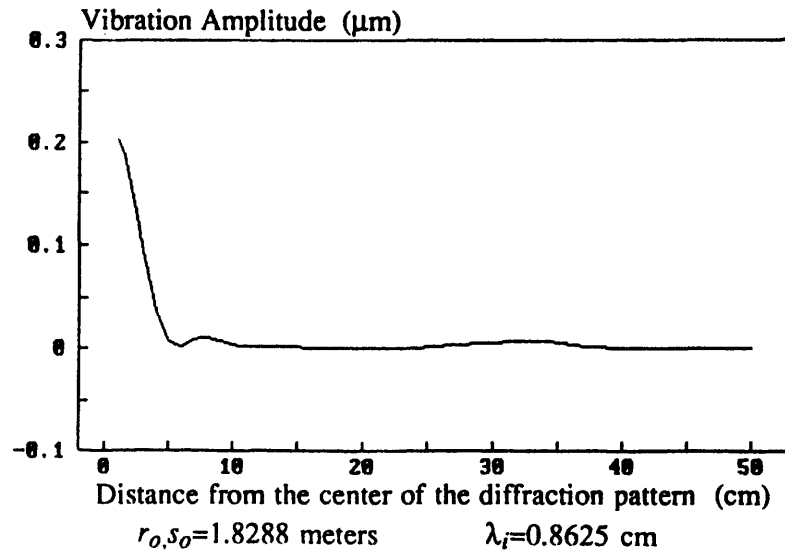


Figure 4.15 Calculated diffraction pattern for the sixth fundamental mode of vibration using a 40 khz sound wave.



Zoom Diffraction Pattern for the 6<sup>th</sup> Fundamental Mode of Vibration  
 Vibration Amplitude ( $\mu\text{m}$ )

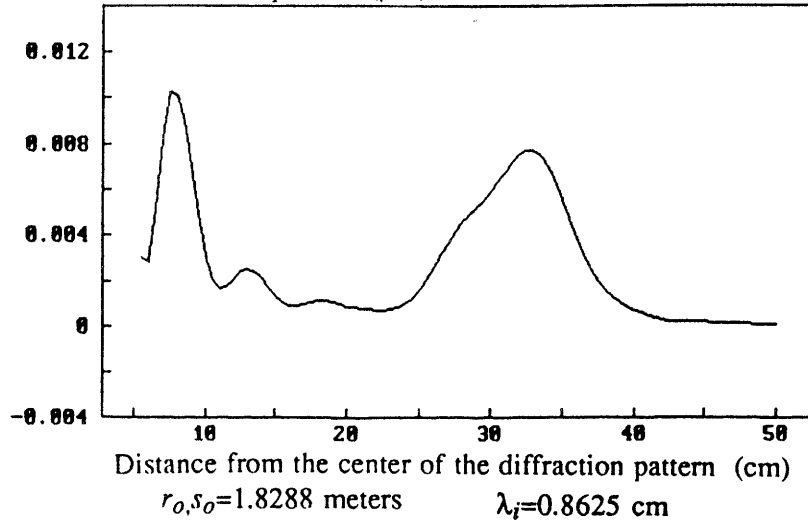


Figure 4.16 Zoom view of the calculated diffraction pattern for the sixth fundamental mode of vibration using a 40 khz sound wave.

Diffraction Pattern for the 6<sup>th</sup> Fundamental Mode of Vibration  
 Vibration Amplitude ( $\mu\text{m}$ )

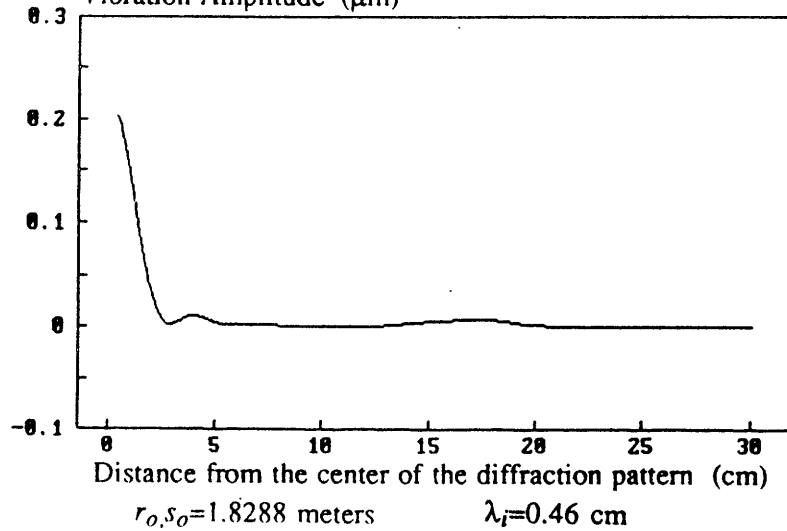


Figure 4.17 Calculated diffraction pattern for the sixth fundamental mode of vibration using a 75 khz sound wave.

Zoom Diffraction Pattern for the 6<sup>th</sup> Fundamental Mode of Vibration  
 Vibration Amplitude ( $\mu\text{m}$ )

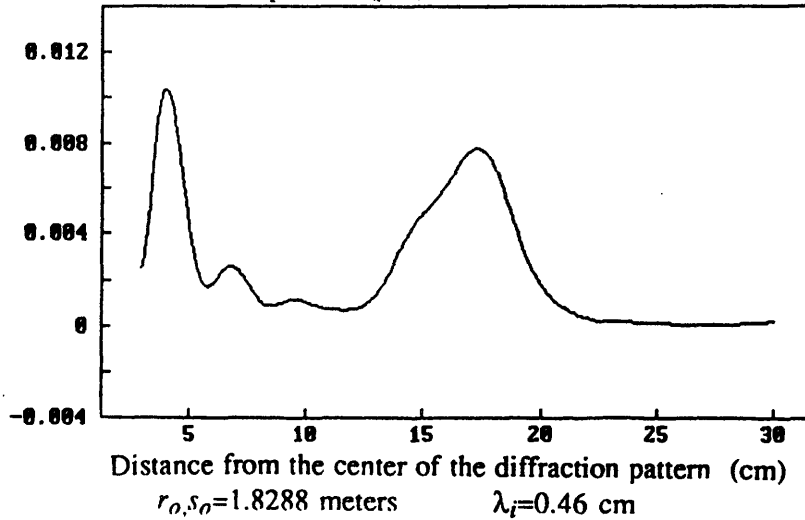


Figure 4.18 Zoom view of the calculated diffraction pattern for the sixth fundamental mode of vibration using a 75 khz sound wave.

The large value of the vibration amplitude at the center of the diffraction pattern is a result of the zeroth order Bessel function acting on each wavenumber present in the calculated wavenumber distribution. This would indicate a large DC vibration amplitude, which is not actually present. For a given argument, the amplitude of the zeroth order Bessel function is much larger than that of the first order. This causes the unrealistic large peak to be predicted in the center of the diffraction pattern. This center peak has side lobes, whose amplitude is on the order of the amplitude of the peak due to the surface wave. Neither the center peak nor its side lobes should be expected in the surface wavenumber distribution and should be subsequently ignored. These plots will be compared to the measured diffraction patterns.

## 5. Results

### 5.1 Experimental Observations

In the course of scanning the diffraction pattern to detect these peaks in frequency modulation, it was found that the amplitudes of the FM signals displayed on the signal analyser were of low level and varying in magnitude. This was found to be due to the fact that the maximum vibration amplitudes were a small percentage of the incident wavelength. The small amplitude is associated with a very small surface velocity with respect to the speed of sound, and generates a small amount of frequency modulation. (See Table 5.1). This unfortunate fact was due to the restriction of plane incident wavefronts, which forced the use of the lower frequency transducers and caused the incident wavelength to be too large.

Vibration Frequency (hz)	Maximum Vibration Amplitude as a Percentage of Incident Wavelength	
	40 KHz	75 KHz
1234	1.60%	3.00%
1706	0.50%	1.00%
3202	0.30%	0.17%

Table 5.1 Maximum amplitude of vibration as a percentage of the incident wavelength.

In addition to this, it was also noted that an amplitude modulation was introduced into the reflected waves at the vibration frequency. The magnitude of

the induced amplitude modulation was observed to be between zero and forty percent of the amplitude of the reflected wave. The measurement system was tested for its sensitivity to amplitude modulation and the results are presented in Table 5.2. These results show that the measurement system is quite insensitive to amplitude modulation in the reflected sound waves. The vibration amplitude measurements were not affected by this unexpected phenomenon.

Amount of Amplitude Modulation as a Percentage of the Maximum Signal Amplitude (%)	Amount of Induced Frequency Modulation Due to the Amplitude Modulation in the Reflected Wave (dB)
90	≈ 10
50	≈ 5
30	≈ 1
10	—

Table 5.2 Effect of amplitude modulation on the frequency modulation measurements.

## 5.2 Diffraction Pattern Measurements

The amplitude of the frequency modulation introduced into the reflected waves at the vibration frequencies of 1706 hz and 3202 hz was so low that repeatable measurements of the diffraction pattern produced by these modes of vibration were not obtained. However, at 1234 hz some repeatable measurements were obtained. The FM measurements made using the 40 khz transducer were more stable than those made with the 75 khz transducer. This fact was attributed to the larger overall signal to noise level of the reflected sound waves at 40 khz.

The results of the diffraction pattern measurements are displayed below in Figures 5.01 and 5.02.

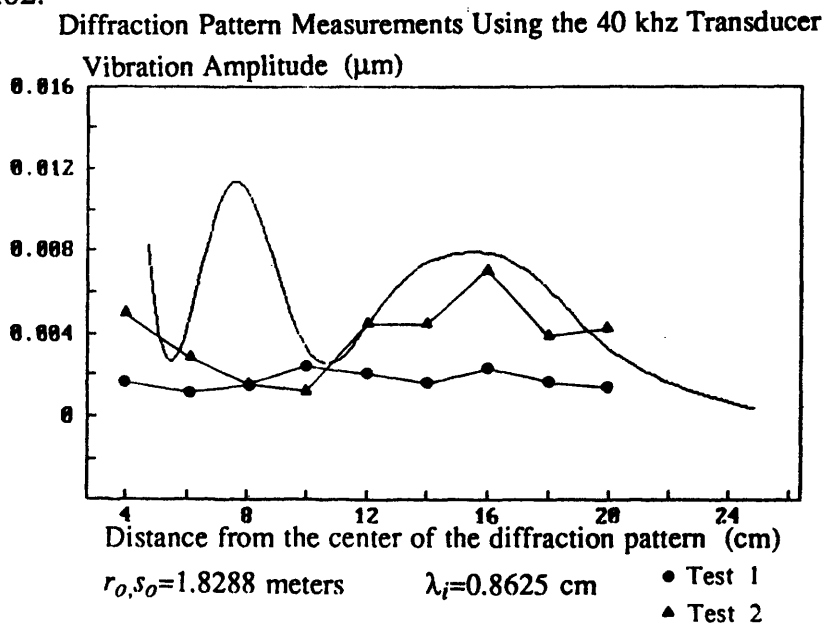


Figure 5.01 Diffraction pattern measurements using the 40 khz transducer.

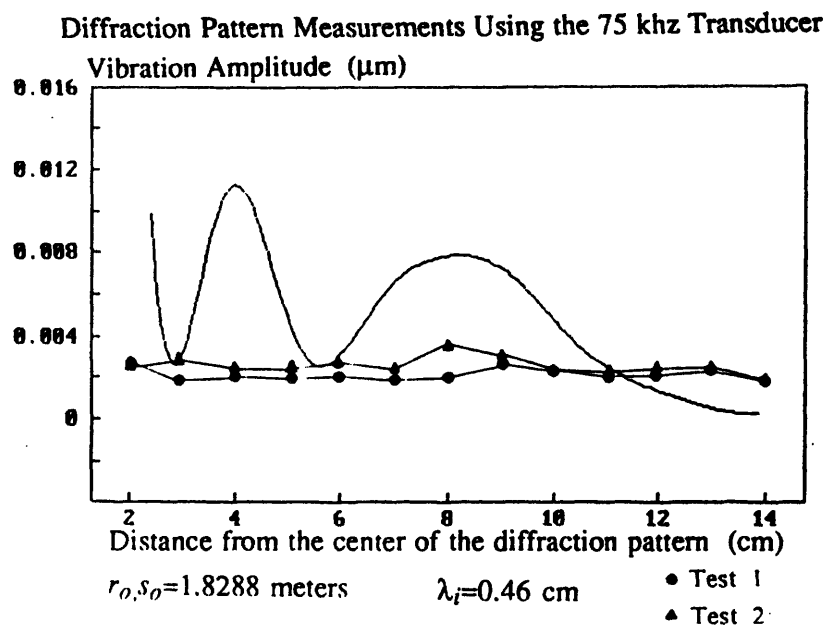


Figure 5.02 Diffraction pattern measurements using the 75 khz transducer.

## 6. Conclusions and Future Recommendations

### 6.1 Discussion of Results

As can be seen in Figures 5.01 and 5.02, the results agree quite well with the theoretical predictions with respect to the position of the peaks in the diffraction pattern. The amplitudes of these peaks, however, are much smaller than expected by the doppler shift calculations. This can be due to the following. First, the vertical mode shape of the vibrating plate will cause the generated peaks in the diffraction pattern to be located off the horizontal axis. Although the vertical mode shapes were not measured, they were inferred from the bending wavelength associated with the input frequency and the horizontal mode shape. The diffraction pattern was scanned off the horizontal axis in search of the larger amplitude peaks. This search was unsuccessful in measuring larger amplitude peaks in the diffraction pattern, but was successful in locating the peaks as predicted by the theory. Second, the signal levels of the FM component of the reflected waves were only about 5 to 8 decibels above the noise floor. This low signal to noise ratio could be causing some of this discrepancy. Third, the amplitude of the reflected waves in the diffraction pattern also varies with position. When the amplitude of the reflected wave becomes very small the total signal to noise ratio also becomes very low. This could also be contributing to the incorrect amplitude readings. Fourth, the mode of vibration which was tested contained only three half wavelengths of the vibrating surface wave. The amount of frequency modulation induced into the reflected sound waves is probably

dependent on the number of full surface waves present on the test surface just as the wavenumber resolution is. Therefore, another problem contributing to the amplitude mismatch could be due to the few number of complete surface waves on the test surface.

Despite the fact that the method was tried on only a single mode of vibration, the results look promising. The position of the peaks in the diffraction pattern were shown to be in agreement with the theoretical predictions. The amplitude measurements did not follow the theory, but there are some good indications of signal to noise problems which could cause this. The accuracy of the entire experiment is driven by the chosen transducer. The limits of the experimental setup are solely due to the difficulty in finding appropriate transducers. As stated in section 4.2, the chosen transducers were the best commercially available and were suitable to test the feasibility of this measurement system. There are some ideas for improvements to this measurement system for future work, which focus around improving the ultrasonic transducers. These ideas are discussed in the following section.

## **6.2 Recommendations for Future Research**

The work in this thesis has shown the feasibility of using the diffraction characteristics of an incident wave field to measure the complete wavenumber distribution of a vibrating surface. The results have also brought about some recommendations for future work which can help to fully develop this method.

These improvements to the existing experimental setup are necessary to allow this measurement method to be used in practice.

The two problem areas which require further work are increasing the overall signal to noise ratio and increasing the frequency modulation signal to noise ratio. A transducer, which outputs a higher amplitude and frequency sound wave than was used in this thesis, will improve both signal to noise ratios. From the tests that were performed with the tweeter, it seems possible to generate a larger output with a specially designed or even a high grade commercial tweeter. The limiting factor in finding a suitable tweeter will most likely be its operating frequency range, but the possibility of using some type of tweeter as the source of the incident field still merits some investigation.

To increase the frequency modulation signal to noise ratio, the following idea should be explored. A lock-in amplifier should be tried instead of the frequency meter and discriminator to make the FM measurement. Past experience with these types of amplifiers indicate their possible benefits, with respect to FM signal to noise ratio, over the current method.

If the optimum transducers produce signal to noise ratios which are still too low to accurately make the measurement, then two other options should be investigated to remedy these problems. The large output amplitude of the transducer is needed so that it may be placed far enough away from the vibrating surface to generate plane wavefronts. This restriction may be relaxed if the



possibility of using incident spherical wavefronts is considered. The effect of these waves on the diffraction pattern could be calculated and possibly subtracted out of the measurement. If this turns out to be a feasible thing to do, then the overall signal to noise ratio problem is eliminated by simply moving the transducers closer to the test surface. An investigation into this idea will also provide some insight into the similar problem of finding the diffraction pattern produced by the hull of a cylindrical body, such as a submarine. This is a desired future extension of the work in this thesis.

In the results section, it was noted that in addition to frequency modulation, the reflected sound waves also contained a substantial amount of amplitude modulation at the vibration frequency. This indicates that the mechanism by which the amount of radiating energy that is introduced into the reflected waves as frequency modulation might be different than expected. That is, the doppler shift equation might be a function of the number of surface waves present on the test surface as well as the vibration frequency. In addition to this, it appears that a much larger amount of amplitude modulation is introduced into the reflected waves. Therefore, the physical mechanism by which both forms of modulation are introduced into the diffraction pattern should be investigated fully. Perhaps, a measurement of the amplitude modulation may be used in conjunction with the frequency modulation measurement to indicate the surface wavenumber amplitude in the diffraction pattern measurement.

To improve the results, the entire experiment should be carried out under water. The increased speed of sound in water should improve the overall signal to noise ratio in the following way. Although the operating frequency for a given incident wavelength will increase, the amount of attenuation of the sound wave with distance will decrease. Therefore, the source and receiver may be placed a greater distance away from the vibrating plate. This will cause the incident wavefronts to appear more plane and should improve the results. It is also possible to generate higher sound pressure levels in water than it is in air. Since many experiments in structural acoustics are carried out under water, this is probably where this measurement system should be developed.

## REFERENCES

[1] Petr Beckman and Andre Spizzichino, "The Scattering of Electromagnetic Waves from Rough Surfaces", Artech House, Inc., Norwood, Ma, 1987.

[2] Miles V. Klein, "OPTICS", John Wiley & Sons, New York, 1970.

[3] Leo Levi, "APPLIED OPTICS, A Guide to Optical System Design/Volume 1", John Wiley & Sons, New York, 1968.

[4] Williams and Becklund, "OPTICS: A Short Course for Engineers and Scientists", John Wiley & Sons, New York, 1972.

[5] Jurgen R. Meyer-Arendt, "Introduction to Classical and Modern Optics", Prentice-Hall Inc., New Jersey, 1972.

[6] Francis A. Jenkins & Harvey E. White, "Fundamentals of Optics", McGraw-Hill Inc., New York, 1976.

[7] Milton Abramowitz and Irene A. Stegun, "Handbook of Mathematical Functions with Formulas, Graphs, and Mathematical Tables", National Bureau of Standards, Washington, D.C., Tenth printing 1972.

[8] I. S. Gradshteyn and I. M. Ryzhik, "Table of Integrals, Series, and Products", Academic Press, New York, 1980.

## APPENDIX A



**Massa  
Products  
Corporation**

280 Lincoln Street, Hingham, Massachusetts 02043  
Tel: 617-749-4800 • TWX: 710-348-6932 • FAX: 617-740-2045

## Model TR-89/B Series Types: 23,31,40

### Description

#### TR-89/B

The TR-89/B Series Transducers are rugged electroacoustic devices designed for the efficient generation of ultrasonic energy in air. They are ideally suited for a wide variety of low power, general purpose applications such as ultrasonic intrusion alarms, proximity detection devices, remote control devices and energy management systems.

The transducers consist of a one piece housing with integral diaphragm. This provides a moisture-proof unit, suitable for both indoor and outdoor use when mounted so that the rear terminals are protected from exposure to the direct outdoor environment. The units operate at resonance on the first harmonic overtone. This affords greater efficiency (higher transmitting and receiving response) than an equivalent size device operating at its fundamental.

The standard TR-89/B, Type 23, provides peak untuned receiving response at  $23 \text{ kHz} \pm 2 \text{ kHz}$ . The standard TR-89/B, Type 31 and Type 40, provide peak untuned receiving responses at  $31 \text{ kHz}$  and  $40 \text{ kHz} \pm 2 \text{ kHz}$  respectively. The units provide different directional characteristics at the various frequencies and provide greater range at the lower frequencies due to the attenuation characteristics of sound in air. Thus, the TR-89/B family offers the user a choice of units whose characteristics will match any requirement. Special frequencies, matched transmitting and receiving pairs and other custom features are available on special order (consult factory). There are several million TR-89/B transducers in use in a variety of applications throughout the world.

Massa Products Corporation is a leading designer and manufacturer of a wide variety of electroacoustic transducers and systems for use in air and underwater with over 35 years of specialized experience in the field.

### Model TR-89/B Series



Actual Size 1" Dia  
Shown Twice Actual Size

### APPLICATIONS

- Robotics
- Liquid Level Measurement
- Intrusion Alarms
- Remote Controls
- Proximity Detection
- Solid Level Measurement
- Energy Management Systems

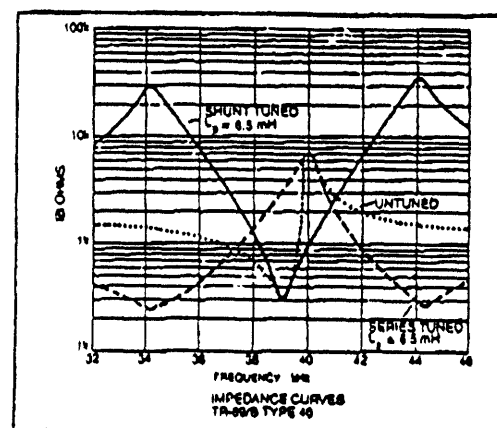
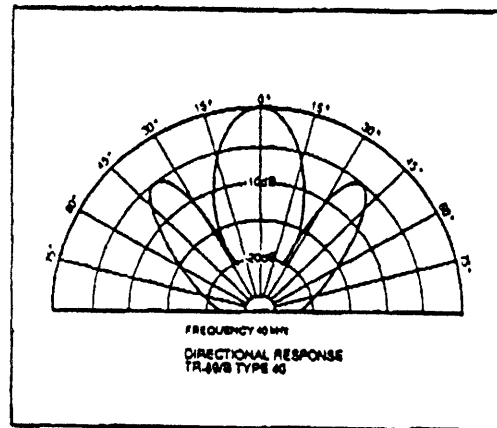
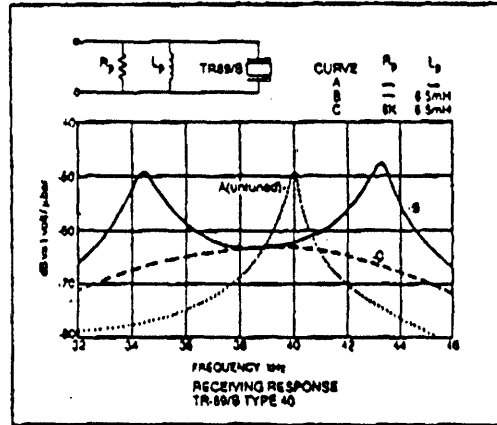
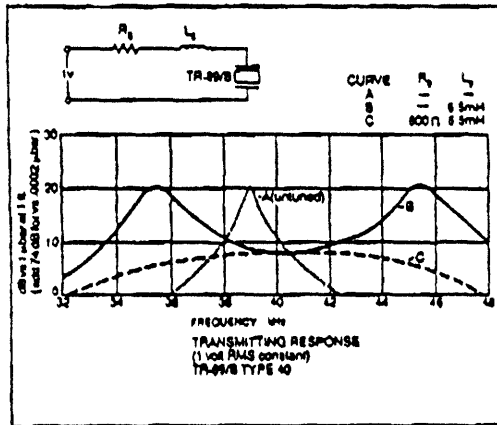
### FEATURES

- Low Cost
- Rugged Packaging
- Moisture-Proof
- High Sensitivity

MASSA Ultrasonic Products are protected by the following patents:  
Patents: 3,510,608; 3,570,995; 3,630,071; 3,697,831; 3,777,831;  
3,777,832; 3,777,833; 3,777,834; 3,777,835; 3,777,836; 3,777,837;  
3,937,995; 3,938,390; 4,017,475; 4,018,408; 4,077,800; 4,107,200;  
4,121,567; 4,128,370; 4,140,781; 4,152,783; 4,156,317; 4,156,318;  
4,251,485; 4,297,510; and others. Please consult the factory for details.

# TYPE 40

## PERFORMANCE CHARACTERISTICS



## Model TR-89/B Series

### Specifications

	Type 23	Type 31	Type 40
Frequency at Maximum Impedance	23 kHz ± 2 kHz	31 kHz ± 2 kHz	40 kHz ± 2 kHz
Bandwidth, Transmitting*			
Tuned	5 kHz	8 kHz	10 kHz
Untuned	3 kHz	3 kHz	5 kHz
Transmitting Sensitivity* dB vs 1 $\mu$ bar per volt at 1 foot (untuned)	+25	+25	+22
Receiving Sensitivity* dB vs 1 volt per $\mu$ bar (untuned)	-41	-41	-50
Rated Power	200mW	200mW	200mW
Maximum Rated Voltage	35 V p p (Square Wave Input) 45 V p p (Sine Wave Input)		
Total Beam Angle* (-3dB Points)	35°	25°	20°
Weight	0.2 oz.	0.2 oz.	0.2 oz.

All Specifications typical at 22°C and subject to change without notice

\*See Performance Characteristics

### Options

- 1 Closer Frequency Tolerances
- 2 Different Operating Frequencies
- 3 Water Tight Unit with Integral Cable
- 4 Phono connector

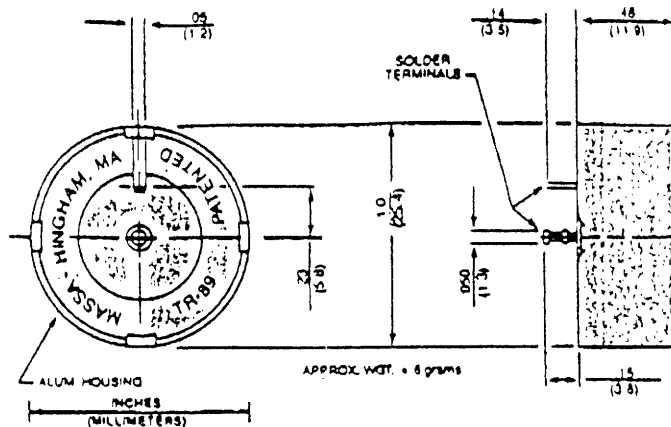
All Options at Extra Cost and Subject to Minimum Order Requirements



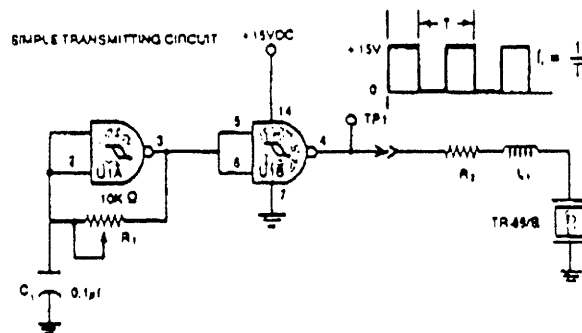
**Massa Products Corporation**  
280 Lincoln Street  
Hingham, Massachusetts 02043

Tel 617-749-4800  
TWX: 710-348-6932  
FAX: 617-740-2045

### Outline Dimensions



### Applications Circuit



TRANSMITTING FREQUENCY	TRANSDUCER		
23 kHz ± 2 kHz	TR-89/B TYPE 23	820 $\Omega$	7 mH
31 kHz ± 2 kHz	TR-89/B TYPE 31	310 $\Omega$	12 mH
40 kHz ± 2 kHz	TR-89/B TYPE 40	520 $\Omega$	8.5 mH

### NOTES:

1. U1 is a National Semiconductor CD 4093B Quad 2 input NAND Schmitt Trigger or equivalent.
2. R1 must be a 10 turn wire wound precision potentiometer.
3. Adjust R1 for correct frequency ( $f_1$ ) at TP1.

Represented By:





**Massa  
Products  
Corporation**

280 Lincoln Street, Hingham, Massachusetts 02043  
Tel: 617-749-4800 • TWX: 710-348-6932 • FAX: 617-740-2045

## MODELS E-152/40 E-152/75 BROAD BEAM ULTRASONIC TRANSDUCER

### Description

#### E-152/40

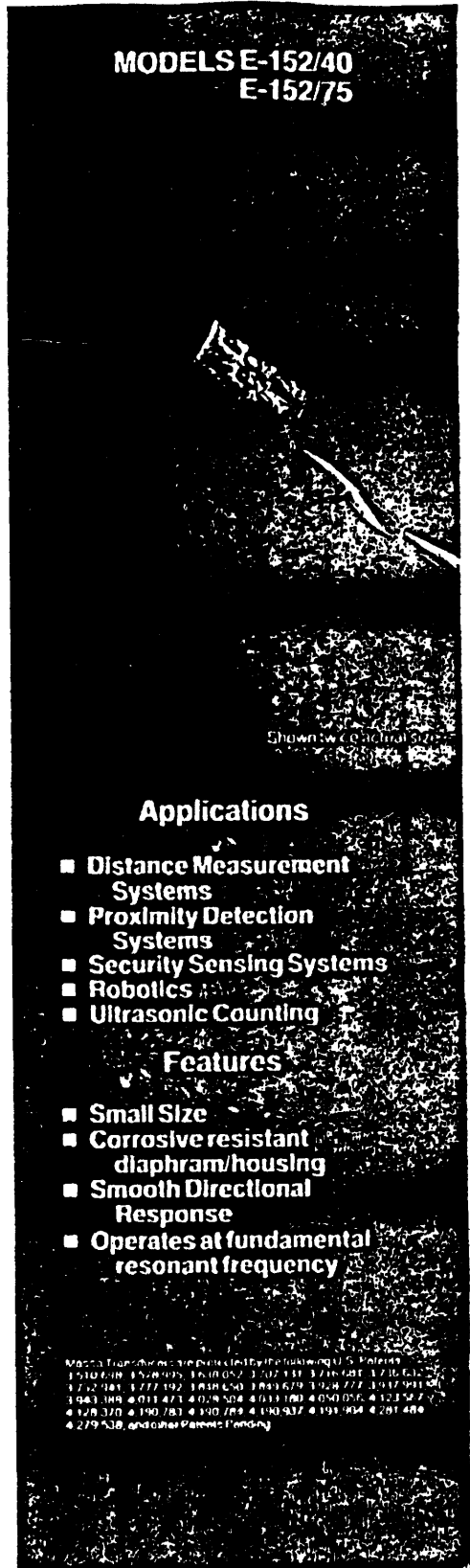
The Massa Model E-152/40 is a miniature air ultrasonic transducer having many applications in short range sensing and remote control where non-contact is desired. The transducer operates at 40 kHz, its fundamental resonant frequency, thereby producing a relatively broad directional response, free of minor lobes. The housing and diaphragm are one piece and made from stainless steel to provide high resistance to corrosive atmospheres. Each transducer is provided with 2 feet of twisted pair cable potted at the back of the housing. Other lengths of cable or different terminations are available on special order. An external horn may be attached to reduce the beam angle for highly directional applications and maximum range.

#### E-152/75

The Massa Model E-152/75 is physically the same as the E-152/40 but operates at 75 kHz. Operation at 75 kHz permits better resolution and performance in short range applications.

Massa Products Corporation is a leading designer and manufacturer of a wide variety of electroacoustic transducers and systems for use in air and underwater, with over 35 years of specialized experience in this field.

**MODELS E-152/40  
E-152/75**



Shown with control system

### Applications

- Distance Measurement Systems
- Proximity Detection Systems
- Security Sensing Systems
- Robotics
- Ultrasonic Counting

### Features

- Small Size
- Corrosive resistant diaphragm/housing
- Smooth Directional Response
- Operates at fundamental resonant frequency

Massa Products Corporation is a leading designer and manufacturer of a wide variety of electroacoustic transducers and systems for use in air and underwater, with over 35 years of specialized experience in this field.

# Models E-152/40 E-152/75

## Specifications

	E-152/40	E-152/75
Frequency at Receiving Sensitivity	40 kHz ± 2 kHz	75 kHz ± 2 kHz
Bandwidth Tuned	14 kHz	20 kHz
Untuned	1 kHz	1 kHz
Transmitting Sensitivity (d0 vs 1 $\mu$ bar per volt at 1 foot untuned)	+ 10	+ 10
Receiving Sensitivity (dB vs 1 volt $\mu$ bar untuned)	- 57	- 62
Rated Power	10mW	10mW
Nominal Impedance at minimum resonance	1000 $\Omega$	1000 $\Omega$
Total Beam Angle (3dB) Conical	75°	60°
Operating Temperature	0-70°C	0-70°C
Humidity	0-90%	Non condensing
Weight	5 grams	6 grams

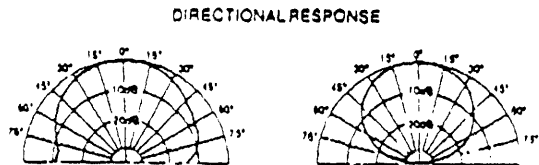
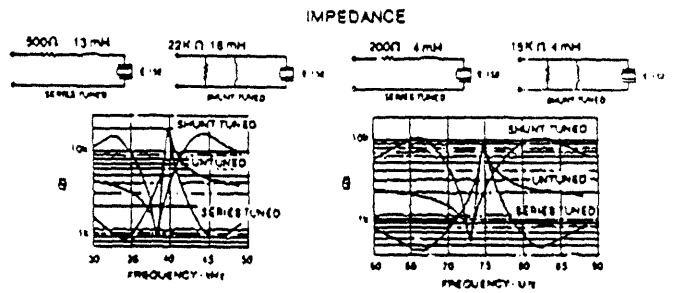
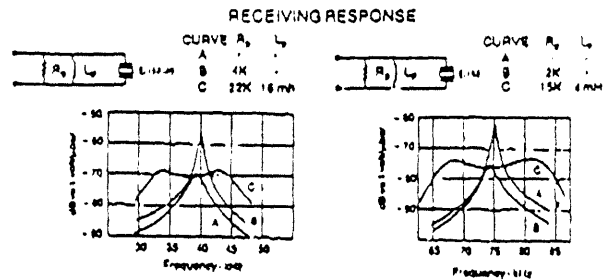
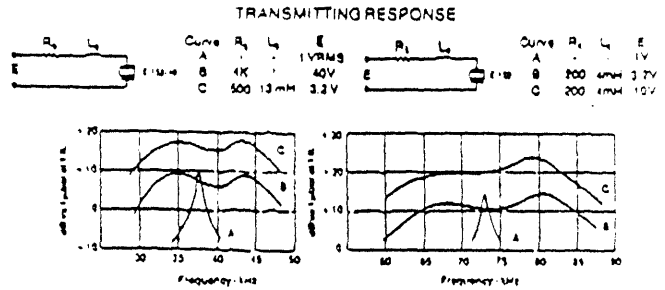
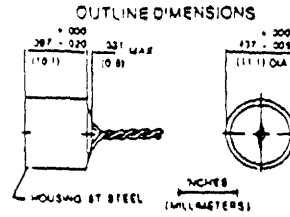
All specifications typical at 22°C and barometric pressure of 751mm of mercury and subject to change without notice



## Massa Products Corporation

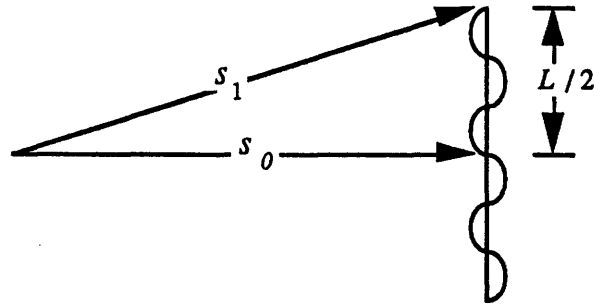
280 Lincoln Street  
Hingham, Massachusetts 02043

Tel: 617-749-4800  
TWX: 710-348-6932  
FAX: 617-740-2045



Represented By:

### Indication of How Close to Plane are the Incident Waves



$$L = 15 \text{ cm}$$

$$s_0 = \frac{\text{Total Travel in Air}}{2}$$

$$s_1 = \sqrt{s_0^2 + \frac{L^2}{4}}$$

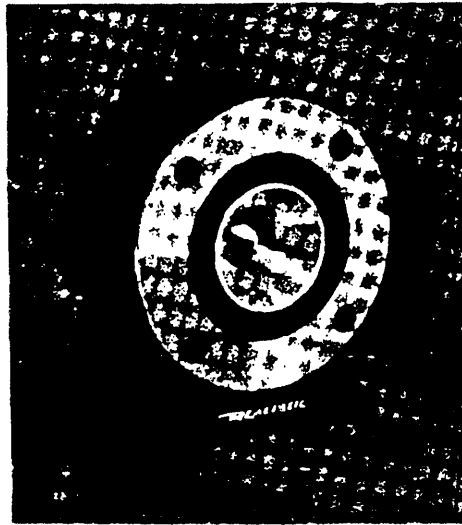
Frequency (hz)	Incident Wavelength (cm)	Total Travel in Air (cm)	So (cm)	(S1-So)/Incident Wavelength (%)
40	0.86	457.2	228.6	14.3
75	0.46	335.3	167.6	36.5
150	0.23	228.6	114.3	106.9
215	0.14	137.2	68.6	292.1

The numbers in the last column indicate how much later the points on the edge of the plate see the waves from the source than those in the center do. At 150 khz, the phase difference between points in the center of the plate and those on the edge is almost a full wavelength.

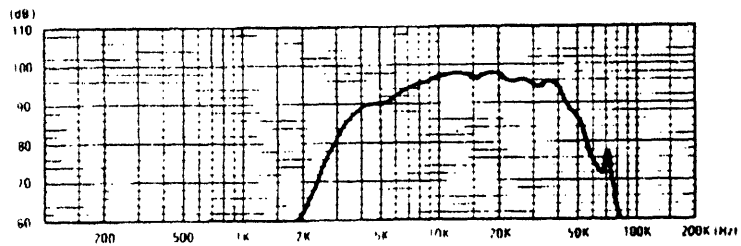
Radio Shack Tweeter Frequency Response

**REALISTIC<sup>®</sup>**

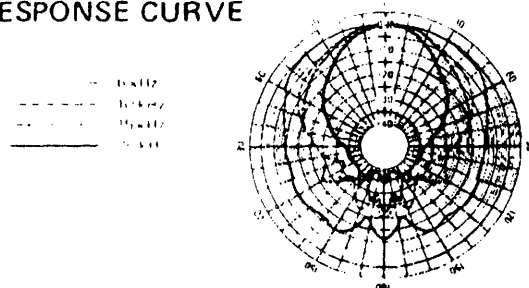
Enhance the Performance of ANY Stereo System  
with this  
**SUPER TWEETER**  
Cat. No. 40-1310B



**FREQUENCY RESPONSE CURVE**

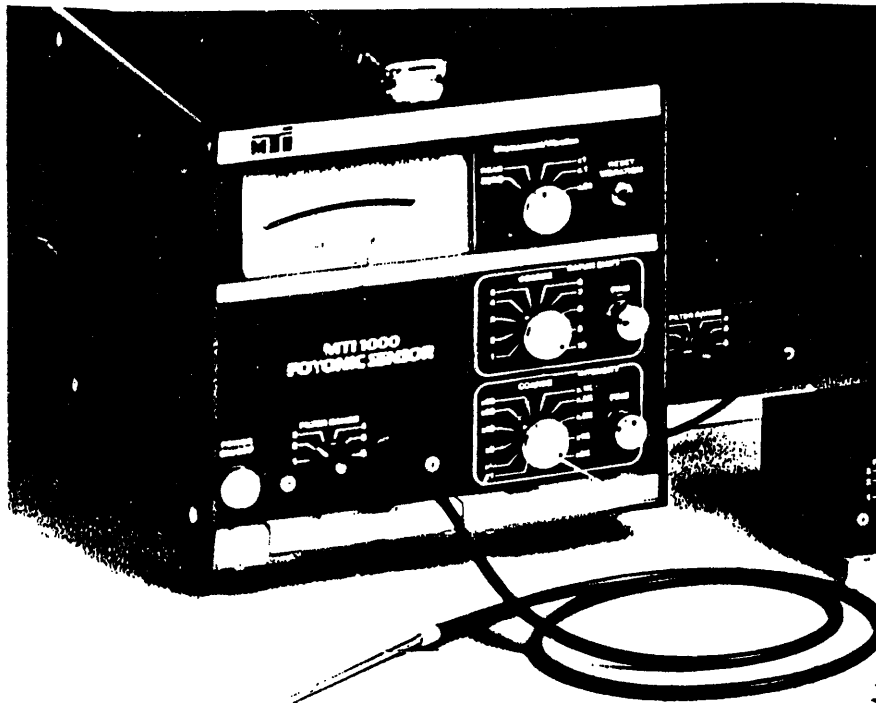







**POLAR RESPONSE CURVE**



## APPENDIX B

# Mechanical Technology Incorporated Fotonic Sensor Specifications



<b>PROBE/PLUG-IN MODULE</b>	<p>Probe Operating Temperature Range -100 to 300°F</p> <p>Probe Tip Length 3 in.</p> <p>Probe Minimum Bend Radius 1 in.</p> <p>Typical Probe Operating Pressure Range Vacuum of 29 in. Hg to 300 psig</p>	<p>Range, Standoff, Frequency Response Refer to Specification Chart</p> <p>Calibration Data Sensitivity and frequency response characteristics supplied with each module</p>
<b>VIBRATION READOUT</b>	<p>Ranges ±1-10 V peak-to-peak full scale ±.1-1 V peak-to-peak full scale ±.01-0.1 V peak-to-peak full scale</p> <p>Accuracy ±1 Range—Accurate to within 1% ±.1 Range—Accurate to within 1% ±.01 Range—Accurate to within 10%</p> <p>Offset Less than 0.5% of full scale*</p> <p>Frequency Response ±1 Range—Flat within 1% from 10 Hz to 100 kHz ±.1 Range—Flat within 1% from 20 Hz to 100 kHz ±.01 Range—Flat within 1% from 60 Hz to 100 kHz</p>	<p>Stability—60 to 95°F ±1 Range—Drift less than 0.1% of range ±.1 Range—Drift less than 0.5% of range ±.01 Range—Drift less than 5% of full range</p> <p>Vibration Output Signal: 10 V dc full scale signal on each range 100 Ω output impedance</p> <p>Displacement Output Signal ±10 V dc, 100 Ω output impedance</p>
<b>DISPLACEMENT READOUT</b>	<p>Stability—12 Hours (± 2°F) Drift less than 0.1% of full scale*</p> <p>Stability—60 to 95°F Drift less than 1% of full scale*</p>	<p>Displacement Output Signal ±10 V dc, 100 Ω output impedance</p>
<b>GENERAL</b>	<p>Line Voltage Stability—105 to 130 V ac Drift less than 0.1% of full scale*</p> <p>Instrument Operating Temperature Range 60 to 150°F</p> <p>Storage Temperature Range 0 to 150°F</p> <p>Readout 3½-in. test band meter</p>	<p>Power Requirements Less than 10 W, 115/230 V, 50 to 400 Hz</p> <p>Dimensions Weight: 8 lbs. Stact H = 7 in., W = 7½ in., L = 10 in.</p> <p>*Full range=Full scale deflection on unscaled range, 10 V dc.</p>
<b>FIBER DISTRIBUTION</b>	<div style="display: flex; justify-content: space-around; align-items: center;"> <div style="text-align: center;">  <p>○ Transmitting Fiber</p> </div> <div style="text-align: center;">  <p>● Receiving Fiber</p> </div> <div style="text-align: center;">  <p>Random (R) Sensing response with broad displacement range.</p> </div> <div style="text-align: center;">  <p>Hemispherical (H) Long range with limited displacement sensitivity.</p> </div> <div style="text-align: center;">  <p>Concentric Transmittal Ingege (CTI) Intermediate range between Random and Hemispherical.</p> </div> </div>	

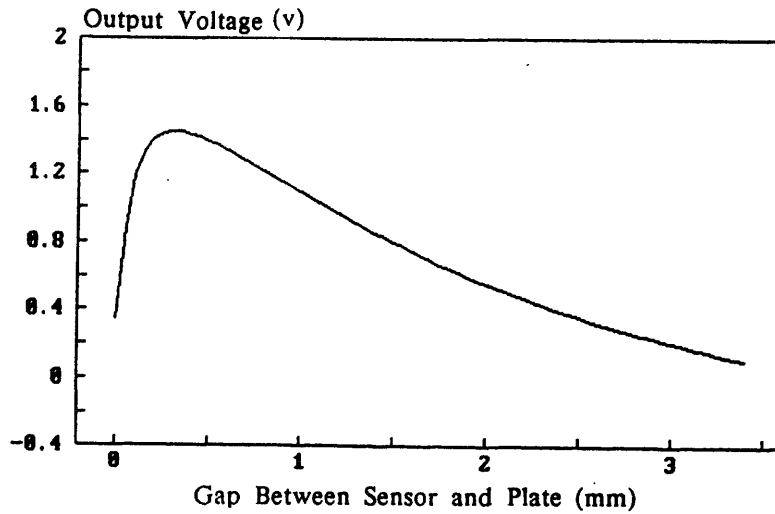
MTI INSTRUMENTS DIVISION 958 Albany-Shaker Road, Latham, NY 12110  
(518) 786-7711 1-800-839-6210 (outside New York State)  
1-800-543-4017 (inside New York State)



4-87

## Fotonic Sensor Calibration Curve

Calibration Curve for the Photonic Sensor on the Aluminum Plate



Gap (mm)	DC Voltage (volts)
0.00	0.528
0.05	1.009
0.10	1.256
0.15	1.371
0.20	1.426
0.25	1.445
0.30	1.446
0.35	1.436
0.40	1.418
0.45	1.394
0.50	1.368
0.55	1.339
0.60	1.309
0.65	1.277
0.70	1.245
0.75	1.212
0.80	1.181
0.85	1.151
0.90	1.119
0.95	1.086
1.00	1.055
1.05	1.024
1.10	0.993

Gap (mm)	DC Voltage (volts)
1.15	0.962
1.20	0.932
1.25	0.902
1.30	0.872
1.35	0.843
1.40	0.815
1.45	0.788
1.50	0.761
1.55	0.734
1.60	0.709
1.65	0.685
1.70	0.661
1.75	0.637
1.80	0.613
1.85	0.59
1.90	0.568
1.95	0.546
2.00	0.524
2.05	0.503
2.10	0.483
2.15	0.463
2.20	0.444
2.25	0.425

Gap (mm)	DC Voltage (volts)
2.30	0.406
2.35	0.388
2.40	0.371
2.45	0.354
2.50	0.337
2.55	0.321
2.60	0.304
2.65	0.289
2.70	0.273
2.75	0.258
2.80	0.243
2.85	0.228
2.90	0.214
2.95	0.201
3.00	0.187
3.05	0.175
3.10	0.164
3.15	0.153
3.20	0.141
3.25	0.129
3.30	0.117
3.35	0.106

**APPENDIX C**



Mode shape measurement at a vibration frequency of 1234 hz.

Average peak amplitude of horizontal mode shapes is 83 micrometers.

Distance from Center of Plate (cm)	Scan at 5 cm. above centerline		Scan across the centerline		Scan at 5 cm. below centerline	
	Displacement (micrometers)	Phase vs. Input (deg)	Displacement (micrometers)	Phase vs. Input (deg)	Displacement (micrometers)	Phase vs. Input (deg)
-7.50	9.60	-37.40	8.61	114.00	16.00	-99.20
-7.00	26.76	-38.00	20.10	112.80	36.00	-107.90
-6.50	46.76	-36.00	32.77	111.60	63.88	-103.00
-6.00	67.85	-38.70	46.92	114.50	85.85	-99.70
-5.50	81.85	-37.50	60.31	116.30	106.15	-101.10
-5.00	93.08	-37.50	68.77	118.60	112.31	-101.10
-4.50	89.85	-37.50	72.31	118.30	113.69	-94.20
-4.00	83.23	-37.80	78.15	119.00	116.92	-100.40
-3.50	72.31	-37.60	77.69	114.90	106.31	-100.30
-3.00	57.54	-40.70	63.38	116.00	85.38	-97.00
-2.50	35.54	-39.70	47.85	118.60	67.69	-101.00
-2.00	10.85	-39.40	27.08	117.50	41.38	-93.20
-1.50	8.82	141.50	7.82	105.70	17.08	-87.30
-1.00	27.23	137.40	6.52	-35.70	8.65	67.80
-.50	38.62	140.80	6.38	-37.60	24.77	79.50
.00	42.01	141.70	6.88	98.20	31.54	89.10
.50	41.08	141.40	35.23	118.70	28.92	84.50
1.00	26.92	142.70	55.23	120.70	17.08	76.20
1.50	6.91	148.10	71.54	123.70	6.12	-60.20
2.00	14.15	-44.70	75.54	123.50	26.62	-84.30
2.50	40.92	-41.30	75.54	123.00	54.62	-94.90
3.00	66.15	-40.10	62.01	123.30	82.31	-90.50
3.50	80.46	-37.30	43.54	124.20	110.62	-93.90
4.00	94.46	-38.90	26.46	125.10	125.85	-97.80
4.50	91.23	-40.40	6.55	130.60	136.62	-93.70
5.00	83.23	-39.30	3.65	-67.80	127.69	-96.20
5.50	66.46	-39.70	10.06	-57.10	105.23	-93.00
6.00	50.31	-39.30	13.54	-57.70	87.69	-91.10
6.50	26.92	-38.60	10.01	-53.10	54.77	-89.80
7.00	11.29	-39.50	5.68	-55.00	26.77	-88.30
7.50	.31	-142.40	2.08	-48.00	5.95	-87.10

Mode shape measurement at a vibration frequency of 1706 hz.

Average peak amplitude of horizontal mode shapes is 27 micrometers.

Distance from Center of Plate (cm)	Scan at 5 cm. above centerline		Scan across the centerline		Scan at 5 cm. below centerline	
	Displacement (micrometers)	Phase vs. Input (deg)	Displacement (micrometers)	Phase vs. Input (deg)	Displacement (micrometers)	Phase vs. Input (deg)
-7.50	1.38	-25.50	8.98	-45.00	.78	42.40
-7.00	2.43	-65.80	22.92	-48.70	.42	41.20
-6.50	3.82	-85.60	36.62	-47.70	.27	53.80
-6.00	5.42	-92.90	46.00	-49.30	.83	141.80
-5.50	6.40	-103.20	48.15	-50.00	.98	137.10
-5.00	6.29	-115.30	38.62	-49.70	3.09	134.70
-4.50	4.86	-123.40	20.15	-52.70	3.65	140.30
-4.00	3.97	-121.60	4.80	-53.10	4.60	131.10
-3.50	3.57	-99.30	11.52	122.00	1.82	144.00
-3.00	5.06	-70.40	25.08	117.60	2.29	-53.70
-2.50	9.45	-57.40	29.23	117.60	7.75	-50.00
-2.00	16.00	-52.60	25.38	111.80	17.54	-53.90
-1.50	21.38	-50.30	14.05	109.20	29.38	-52.80
-1.00	28.15	-49.30	1.40	81.70	37.23	-55.00
-.50	32.31	-46.40	1.31	-34.30	42.46	-55.10
.00	33.69	-45.30	1.95	101.30	48.15	-60.50
.50	35.54	-45.70	15.17	107.80	44.46	-61.60
1.00	32.62	-45.60	23.38	121.00	40.15	-62.00
1.50	24.77	-42.20	27.69	125.40	31.08	-61.20
2.00	17.85	-42.80	24.62	107.70	17.85	-64.70
2.50	10.51	-37.30	17.69	130.40	8.82	-66.10
3.00	4.92	-22.30	5.40	130.80	2.06	113.90
3.50	2.78	68.70	9.55	-50.10	11.69	112.90
4.00	5.85	105.40	25.54	-47.50	18.62	112.30
4.50	8.15	109.30	37.54	-48.40	22.46	113.60
5.00	8.88	111.30	41.54	-46.00	22.31	110.50
5.50	7.69	112.30	42.46	-46.00	20.15	117.50
6.00	6.49	110.20	35.54	-47.00	16.92	110.00
6.50	3.60	111.40	23.85	-45.10	12.37	109.60
7.00	2.40	117.10	9.38	-43.30	6.23	113.10
7.50	.59	131.00	.42	91.10	.93	123.40

Mode shape measurement at a vibration frequency of 3202 hz.

Average peak amplitude of horizontal mode shapes is 11 micrometers.

Distance from Center of Plate (cm)	Scan at 5 cm. above centerline		Scan across the centerline		Scan at 5 cm. below centerline	
	Displacement (micrometers)	Phase vs. Input (deg)	Displacement (micrometers)	Phase vs. Input (deg)	Displacement (micrometers)	Phase vs. Input (deg)
-7.50	1.38	65.30	.24	-88.60	.18	74.30
-7.00	2.20	66.70	.18	41.20	.43	103.70
-6.50	2.31	66.40	.27	-33.30	.17	-152.50
-6.00	.23	-2.70	1.68	-90.50	.70	-99.10
-5.50	3.91	-103.50	3.94	-95.70	4.25	-90.90
-5.00	6.40	-103.90	5.40	-99.80	6.60	-88.80
-4.50	6.60	-103.40	5.09	-97.90	7.08	-87.60
-4.00	4.08	-101.60	2.28	-102.70	6.97	-86.20
-3.50	1.26	68.10	4.28	77.40	3.77	-86.60
-3.00	6.40	74.00	11.02	76.80	2.34	-87.70
-2.50	12.37	74.80	14.49	77.50	6.05	90.80
-2.00	14.72	78.00	12.98	79.30	11.02	87.50
-1.50	12.54	76.30	7.52	76.80	11.35	93.80
-1.00	7.00	75.00	2.43	67.20	8.54	89.20
-.50	.34	-54.10	1.86	62.80	2.83	92.60
.00	6.66	-99.90	5.95	78.10	4.66	-80.20
.50	11.46	-99.70	12.54	79.20	8.09	-84.10
1.00	9.28	-99.70	13.88	81.60	8.82	-83.50
1.50	3.37	-98.70	10.57	84.10	6.18	-82.80
2.00	4.89	76.10	3.71	85.20	.83	-79.00
2.50	12.37	79.40	5.00	-97.30	3.82	97.00
3.00	15.06	79.40	10.68	-94.40	6.52	96.10
3.50	14.15	76.80	12.86	-94.20	8.09	88.60
4.00	7.98	79.00	9.66	-94.10	5.37	91.40
4.50	.36	-81.00	2.29	-89.30	.37	75.60
5.00	8.43	-100.80	6.22	76.60	5.42	-90.50
5.50	13.09	-101.90	13.88	79.30	10.00	-91.10
6.00	12.69	-100.30	16.31	81.70	11.08	-90.00
6.50	9.15	-100.60	13.15	80.30	8.37	-90.50
7.00	4.77	-93.60	7.65	79.50	3.77	-87.80
7.50	.36	-7.40	2.20	77.10	.60	-82.20

## APPENDIX D

Turbo Pascal computer program to calculate the expected diffraction pattern.

```
program PLATE_VIBRATION_DIFFRACTION_PATTERN;

{$i input.inc }
{$i haloplot.inc }
{$i modfile.pas }
{$i bessj0.pas }
{$i bessj1.pas }
{$i bessj.pas }

const
    lambda_1 = 0.0046; { meters }
    length = 0.15; { meters }
    rho_o = 1.2; { kg/m**3 }
    c = 345; { meters/sec }
    size = 200;

type
    wavenumber = record
        mag,lambda : real;
        N : integer;
    end;

    wavenumber_array = array[1..size] of wavenumber;

var
    x : wavenumber_array;
    kmin,kmax,delta_k,
    starting_x,
    stopx,so,b,ro,amplitude,
    stepsize,multiplier : real;
    counter,mode : integer;
    source,destin : text;
    filename : string[64];
```

```

procedure CREATE(var k:wavenumber_array; kmin,kmax,deltak,
                amplitude_factor:real; m:integer; var i:integer);

var   check   : integer;
      wave,km  : real;

begin
  newgraph;
  check := m mod 2;
  km    := m*pi/length;
  wave  := kmin;
  i     := 0;
  deltak := (kmax - kmin) / size;
  repeat
    i := i + 1;
    if wave = km then
      k[i].mag := 0.5
    else if (check = 0) then
      k[i].mag := sin(0.5*wave*length)/(0.5*km*length*
                                         (1-sqr(wave)/sqr(km)))
    else
      k[i].mag := cos(0.5*wave*length)/(0.5*km*length*
                                         (1-sqr(wave)/sqr(km)));
    k[i].mag := (sqr(k[i].mag)/0.25) * amplitude_factor *
                lambda_1;

    k[i].lambda := 2*pi/wave;
    k[i].N      := trunc(length/k[i].lambda);
    wave       := wave + deltak;
    plotpoint(wave/100,k[i].mag/lambda_1,1);
  until wave >= kmax;
  displaygraph(1);
  i := i - 1;
end;

function BESSEL(m:integer; c:real):real;

begin
  if m = 0 then BESSEL := bessj0(c)
  else if m = 1 then BESSEL := bessj1(c)
  else BESSEL := bessj(m,c);
end;

```

```

procedure CALCULATE(k:wavenumber_array; counter:integer);

var   Wn,W,x,v,ratio,y,low,high : real;
      i,j,step,number           : integer;

begin
  if starting_x > 0.02 then
    assign(destin,'c:\user\bob\data\acoustic\'+filename+
                                                    '.sm1')
  else
    assign(destin,'c:\user\bob\data\acoustic\'+filename+
                                                    '.big');

  rewrite(destin);
  newgraph;
  x := starting_x;
  ClrScr;
  gotoxy(33,10);
  write('WORKING ');
  gotoxy(15,13);
  write('Distance from center of pattern =      m. ');
  gotoxy(15,16);
  write('Current Wavenumber being calculated = ');
  step := 0;
  repeat
    gotoxy(48,13);
    write(x:6:3);
    step := step + 1;
    j := 0;
    Wn := 0.0;
    W := 0.0;
    for i := 8 to counter do
      begin
        if step = maxint then step := 0;
        step := step + 1;
        gotoxy(53,16);
        write(i:3);
        case (step mod 128) of
          0 ,127 : begin
                    gotoxy(30,10);
                    write('|');
                    gotoxy(42,10);
                    write('|');
                  end;
        end;
      end;
  until false;
end;

```

```

31,158 : begin
        gotoxy(42,10);
        write('\');
        gotoxy(30,10);
        write('/');
    end;
63,189 : begin
        gotoxy(30,10);
        write('-');
        gotoxy(42,10);
        write('-');
    end;
95,221 : begin
        gotoxy(42,10);
        write('/');
        gotoxy(30,10);
        write('\');
    end;
end;
ratio := x*k[i].lambda/(lambda_1*so);
j      := -1;
low    := -0.5;
high   := 0.5;
number := 0;
repeat
    if (ratio>low) and (ratio<high) then j := number
    else begin
        low    := low + 1;
        high   := high + 1;
        number := number + 1;
    end;
until (j=number);
v := 4*pi*k[i].mag/lambda_1;
Wn := sqr(sin((2*k[i].N+1)*pi*k[i].lambda*x/(lambda_1*so))
           /sin(pi*k[i].lambda*x/(lambda_1*so)));
W := W + sqr(BESSEL(j,v)) * Wn * sqr(k[i].lambda);
end;
y := sqr((2 * b * amplitude)/(lambda_1 * so * ro)) * W /
      (rho_o * c);

x := x + stepsize;
writeln(destin,x,y);
plotpoint(x*100,y*multiplier,1);
until (x >= stopx);
close(destin);
displaygraph(1);
end;

```





```

procedure TRIANGLE(var k:wavenumber_array;
                  var counter:integer);

var i : integer;

begin
  counter := size;
  newgraph;
  i := 8;
  repeat
    k[i].lambda := 2*pi/(1250 * (i/counter));
    if i <=(counter/2) then
      k[i].mag := amplitude_factor * lambda_1 *
                (2*i/counter)
    else
      k[i].mag := amplitude_factor * lambda_1 *
                (2 - (2*i/counter));
    k[i].N := trunc(length/k[i].lambda);
    plotpoint((2*pi/k[i].lambda)/100,k[i].mag/lambda_1,1);
    i := i + 1;
  until i = (counter + 1);
  displaygraph(1);
end;

begin {main}
  repeat
    clrscr;
    gotoxy(15,10);
    write('Enter one of the following : ');
    gotoxy(25,12);
    write('"p" to plot existing data');
    gotoxy(25,14);
    write('"c" to calculate and plot new data');
    gotoxy(25,16);
    write('"x" to exit program');
    gotoxy(45,10);
    readln(ch);
    if (ch = 'c') or (ch = 'p') then

```

```

begin
  clrscr;
  gotoxy(15,12);
  write('Enter the name of the file to contain the data.');
```

gotoxy(30,14);  
readln(filename);  
clrscr;

```

end;
if (ch = 'c') then
  begin
    inputdata;
    inputr('Starting X value in pattern',starting_x,'m');
    inputr('Ending X value in pattern',stopx,'m');
    inputr('Stepsize Across the Pattern',stepsize,'m');
    inputr('Smallest wavenumber of interest',kmin,'1/m.');
```

inputr('Largest wavenumber of interest',kmax,'1/m.');

```

    inputi('Mode number of the vibration',mode,'');
    inputr('Max Vibration Amplitude = # * lambda_1',
           amplitude_factor,'');
    inputr('Amplitude of the incident wave',amplitude,'Nt/m');
```

inputr('Distance from the light source',ro,'m');

```

    inputr('Distance to the diffraction pattern',so,'m');
    inputr('Characteristic width of the grating',b,'m');
    inputr('Scaling factor for plot',multiplier,'');
    displayinputdata;
    CREATE(x,kmin,kmax,delta_k,amplitude_factor,mode,counter);
    {
      SINUSOID(x,counter);
      TRIANGLE(x,counter);
    }
    CALCULATE(x,counter);
  end;
  if (ch = 'p') then PLOT;
until(ch = 'x');
clrscr;
end.
```